2017-01-01

Near-Surface and High Resolution Seismic Imaging of the Bennett Thrust Fault in the Indio Mountains of West Texas

Alan Thomas Vennemann
University of Texas at El Paso, atvennemann@miners.utep.edu

NEAR-SURFACE AND HIGH RESOLUTION SEISMIC IMAGING OF THE BENNETT THRUST FAULT IN THE INDIO MOUNTAINS OF WEST TEXAS

ALAN VENNEMANN

Master's Program in Geophysics

APPROVED:

Marianne Karplus, Ph.D., Chair

Terry Pavlis, Ph.D.

Michael T. May, Ph.D.

Charles Ambler, Ph.D.
Dean of the Graduate School

NEAR-SURFACE AND HIGH RESOLUTION SEISMIC IMAGING OF THE BENNETT THRUST FAULT IN THE INDIO MOUNTAINS OF WEST TEXAS

by

ALAN VENNEMANN, B.S.

THESIS

Presented to the Faculty of the Graduate School of

The University of Texas at El Paso

in Partial Fulfillment

of the Requirements

for the Degree of

MASTER OF SCIENCE

Department of Geological Sciences

THE UNIVERSITY OF TEXAS AT EL PASO

December 2017

ACKNOWLEDGEMENTS

First, I would like to thank my advisor, Dr. Marianne Karplus, for taking me on as a student. I came to UTEP without an advisor or a project; she took me in and let me run with research ideas and supported me along the way. She really allowed me to make my graduate education my own and that is a luxury that not many students are afforded. I would like to thank Dr. Terry Pavlis and Dr. Laura Serpa for their support and knowledge along the way. I'd like to thank Galen Kaip, Dr. Steve Harder and all the students that helped me with the field work and data acquisition. It was back breaking work in 100 plus degrees and I wouldn't have been able to do it without each and every one of you.

I would like to thank my family, Tom and Marta Vennemann, my two brothers, Scott and Eric, for supporting me 1500 miles across the country. You've always had my back and supported me in whatever I have done.

Most of all, I would like to thank Thomas Brackman; the man who inspired me to take on geophysics as a career and made it fun. It all started with an undergraduate class at Northern Kentucky University and I was hooked. Without him, I wouldn't have been introduced to my third committee member, Dr. Michael T. May, and for that I am thankful. He imparted many life lessons and his wisdom on me; keep your head down, drive through to get the job done, and don't take bull from anyone. I wouldn't be in the position I am in today if it weren't for him.

ABSTRACT

My research investigates the structure of the Indio Mountains in southwest Texas, 34 kilometers southwest of Van Horn, at the UTEP (University of Texas at El Paso) Field Station using newly acquired active-source seismic data. The area is underlain by deformed Cretaceous sedimentary rocks that represent a transgressive sequence nearly 2 km in total stratigraphic thickness. The rocks were deposited in mid Cretaceous extensional basins and later contracted into fold-thrust structures during Laramide orogenesis. The stratigraphic sequence is an analog for similar areas that are ideal for pre-salt petroleum reservoirs, such as reservoirs off the coasts of Brazil and Angola (Li, 2014; Fox, 2016; Kattah, 2017). The 1-km-long 2-D shallow seismic reflection survey that I planned and led during May 2016 was the first at the UTEP Field Station, providing critical subsurface information that was previously lacking. The data were processed with Landmark ProMAX seismic processing software to create a seismic reflection image of the Bennett Thrust Fault and additional imbricate faulting not expressed at the surface. Along the 1-km line, reflection data were recorded with 200 4.5 Hz geophones, using 100 150-gram explosive charges and 490 sledge-hammer blows for sources. A seismic reflection profile was produced using the lower frequency explosive dataset, which was used in the identification of the Bennett Thrust Fault and additional faulting and folding in the subsurface. This dataset provides three possible interpretations for the subsurface geometries of the faulting and folding present. However, producing a seismic reflection image with the higher frequency sledge-hammer sourced dataset for interpretation proved more challenging. While there are no petroleum plays in the Indio Mountains region, imaging and understanding subsurface structural and lithological geometries and how that geometry directs potential fluid flow has implications for other regions with petroleum plays.

TABLE OF CONTENTS

LIST OF FIGURES

1. INTRODUCTION

Sedimentary rift basins account for approximately 10% to 29% of known hydrocarbon reserves in the world (Beauchamp et al., 1996). Some of those rift basins have been uplifted and interted. Without inversion, there is a wider margin of error when exploring for hydrocarbons; the strata of the basin are inferred to be continuous between rifting structures, and there is simpler and more direct migration of the hydrocarbons from the source to the reservoir and seal. However, basin inversion and compressional shortening along reactivated normal faults redistributes and redirects migration paths of hydrocarbons and other fluids. After the inversion of a sedimentary rift basin, understanding the complex geometry of the structures generated is crucial in determining the optimal location to start production in that basin. The Indio Mountains are analogous to regions with respect to both lithology and tectonic processes that are viable for hydrocarbon exploration and production (Beauchamp et al., 1996).

The Indio Mountains in Hudspeth County, Texas are positioned on the eastern margin of the Chihuahua Trough, a failed rift basin formed in the early Cretaceous (DeFord, 1969; Rohrbaugh, 2001; Haenggi, 2002; Carciumaru and Ortega, 2008; Page, 2011) and additionally represent pre-salt analogues to fruitful reservoirs offshore of Brazil and Angola (Li, 2014; Fox, 2016; Kattah, 2017). The Early Cretaceous rock units record a transition from a terrestrial rift basin to a marginal-marine setting. Laramide-age compression produced overall contractional deformation of the Chihuahua Trough with the genesis of the Chihuahua Tectonic Belt (Haenggi, 2002). Regionally reactivated synrift faults produced shortening in a stacked thrust duplex style resulting in the Bennett and Squaw Peak Thrust Faults as the horse resulting in the Squaw Peak Thrust overrode the horse resulting in the Bennett Thrust (Rohrbaugh, 2001; Page, 2011). These contractional structures were later overprinted by Neogene extension which produced the Indio

Fault, a northwest-southeast trending and southwest dipping normal fault that is exposed in the central Indio Mountains (Rohrbaugh, 2001).

The aims of this study were to investigate the tectonics of the Indio Mountains by acquiring, processing, and interpreting a 1-km-long 2-D shallow seismic reflection line. Along the 1-km line, datasets were collected using 100 150-gram explosive charges and 490 sledge-hammer blows. I processed the data using Landmark's ProMAX software to produce two seismic reflection images for structural interpretation, the first image comprising explosive sources and the second comprising sledge-hammer sources. The Indio Mountains are a structurally complicated area with a number of different faults and folds formed by the processes detailed below. The University of Texas at El Paso (UTEP) owns a research station on a 154 km^2 plot in the Indio Mountain region, 34 km southwest of Van Horn, TX. My Master's thesis included the collection of the first seismic dataset in the Indio Mountains, setting the foundation for more geophysical research. I hypothesized that in addition to the Bennett Thrust Fault expressed at the surface, that there is additional imbricate faulting in the subsurface that is not expressed at the surface. This hypothesis is consistent with work by Page who interpreted imbricate faults at depth based on cross section restorations. My research has identified near-surface structural geometries of the Bennett Thrust Fault and the geometries of additional imbricate faults.

2. Study Area and Regional Geology

2.1 Tectonic History

The Chihuahua Trough is a rift basin that began forming in the Late Jurassic, around 159-156 mya, and lies on the southern part of the North American craton along the United States and Mexico border (Rohrbaugh, 2001; Haenggi, 2002; Carciumaru and Ortega, 2008). The Chihuahua Trough is oriented northwest-southeast bounded by the Aldama Platform to the southwest and by the Diablo Platform to the northeast (Figure 1) (Haenggi, 2002; Carciumaru and Ortega, 2008). The extension developed from northwest Sonora, to southwest Texas and passes through southern New Mexico and northeast Chihuahua (Figure 1) (Haenggi, 2002; Carciumaru and Ortega, 2008). This same Jurassic extensional event is thought to have developed the adjacent Bisbee and Sabinas basins, which make up a portion of the Mexican Borderland rift system (Dickinson and Lawton, 2001; Rohrbaugh, 2001; Haenggi, 2002). The rifting was propagated by either the opening of the Atlantic Ocean, the formation of the Gulf of Mexico or both (Dickinson and Lawton, 2001; Haenggi, 2002; Page, 2011). During the Jurassic, evaporites precipitated in the interior of the basin; however, the details of that deposition are not resolved enough to delineate rapid lateral facies changes and varying thicknesses (Haenggi, 2002). Following the evaporite deposition, the beginning of the Cretaceous marks the deposition of the sediments comprising the conglomerate, sandstone, siltstone, limestone units, as the depositional environment transitioned from a terrestrial rift basin to a lacustrine and marine transgressive sequence (Haenggi, 2002; Page, 2011). All units vary in thicknesses depending on the location within the trough. There is a dramatic thinning of the Cretaceous strata through the trough to the Diablo Platform, which results from series of large displacement, west to south side down, Jurassic normal faults (Carciumaru and Ortega, 2008). Only the Cretaceous rocks are recorded in the Indio Mountains at the surface, and only a portion

of that sequence is being investigated by this research. The Chihuahua trough developed rapidly during the middle-late Jurassic with very little topographic relief; there is no evidence of extensive alluvial fans (Haenggi, 2002). The original extensional faults from the Jurassic persisted and controlled rifting into the Cretaceous (Haenggi, 2002). Throughout this time, sediment influx and basin subsidence were in equilibrium and some boundary faults were observed to displace more than one kilometer. With the exclusion of the northwest portion of the trough, there is no evidence of volcanic activity (Haenggi, 2002).

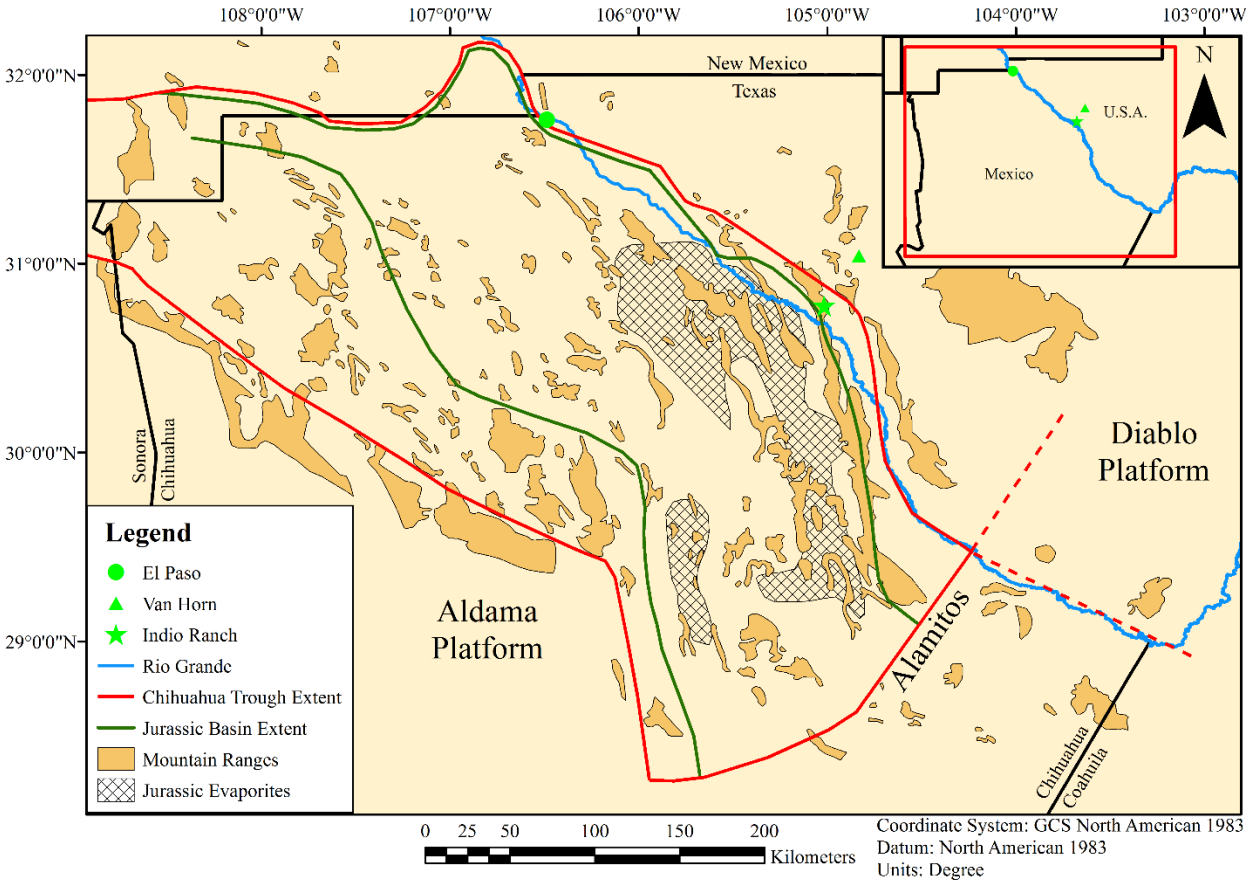

Figure 1: Chihuahua Trough Map
Geologic features of the Chihuahua Trough. Current boundaries are the Aldama Platform and the Alamitos lineament to the west and south and the Diablo Platform to the north and east. Modified after Haenggi (2001) and Carciumaru and Ortega (2008).

The Chihuahua trough was contracted during the Laramide Orogeny, approximately 84-43 mya, as the North American plate overrode the Farallon plate in a general east-west fashion (Figure 2) (Haenggi, 2002; Carciumaru and Ortega, 2008; Page, 2011). This contractional event inverted the sedimentary basin, producing a stacked thrust system including the Bennett and Squaw Peak Thrusts (Figure 3). Regionally however, the style of deformation is variable. In the East Potrillo Mountains in southern New Mexico and the Indio Mountains, thin-skinned deformation is dominant but these thrust systems interacted with Laramide thick-skinned structures (Rohrbaugh, 2001; Carciumaru and Ortega, 2008). For example, the El Paso area records the transitioning of thick to thin skinned deformation with basement involved thrusts in the Franklin Mountains adjacent to the thin skinned deformation just to the south in Sierra Juarez (Rohrbaugh, 2001; Carciumaru and Ortega, 2008). The Jurassic evaporites at the base of the rift also thicken southward into the trough and formed a decollement zone for the contractional faults and detachment folding (Rohrbaugh, 2001; Carciumaru and Ortega, 2008). The consequent fold and thrust belt, which Haenggi (2002) named the Chihuahua Tectonic Belt, trends parallels to the trough's northeast rim. At the surface this transition is marked by the abrupt change from the thick Mesozoic strata of the basin to the Permian aged sedimentary rocks of the Diablo Platform with thin to absent Mesozoic cover (Rohrbaugh, 2001; Carciumaru and Ortega, 2008). The large Jurassic normal faults typically determine the geometry and location of the Laramide contractional faults and folds (Carciumaru and Ortega, 2008).

Thrust faults in the Indio Mountains strike north-northwest and result in stratigraphic repetition of the Cretaceous section. Page (2011) interpreted this general structural pattern as a thrust duplex (Figure 3). A minimum of six km of displacement occurred along thrusts from klippe-fenster relationships (Rohrbaugh, 2001) but Page (2011) estimated 17.3 km of offset from

cross section restorations and hanging-wall cutoffs of the Squaw Peak Thrust. The direction of greatest compression is east-southeast in the southern region of the Indio Mountains

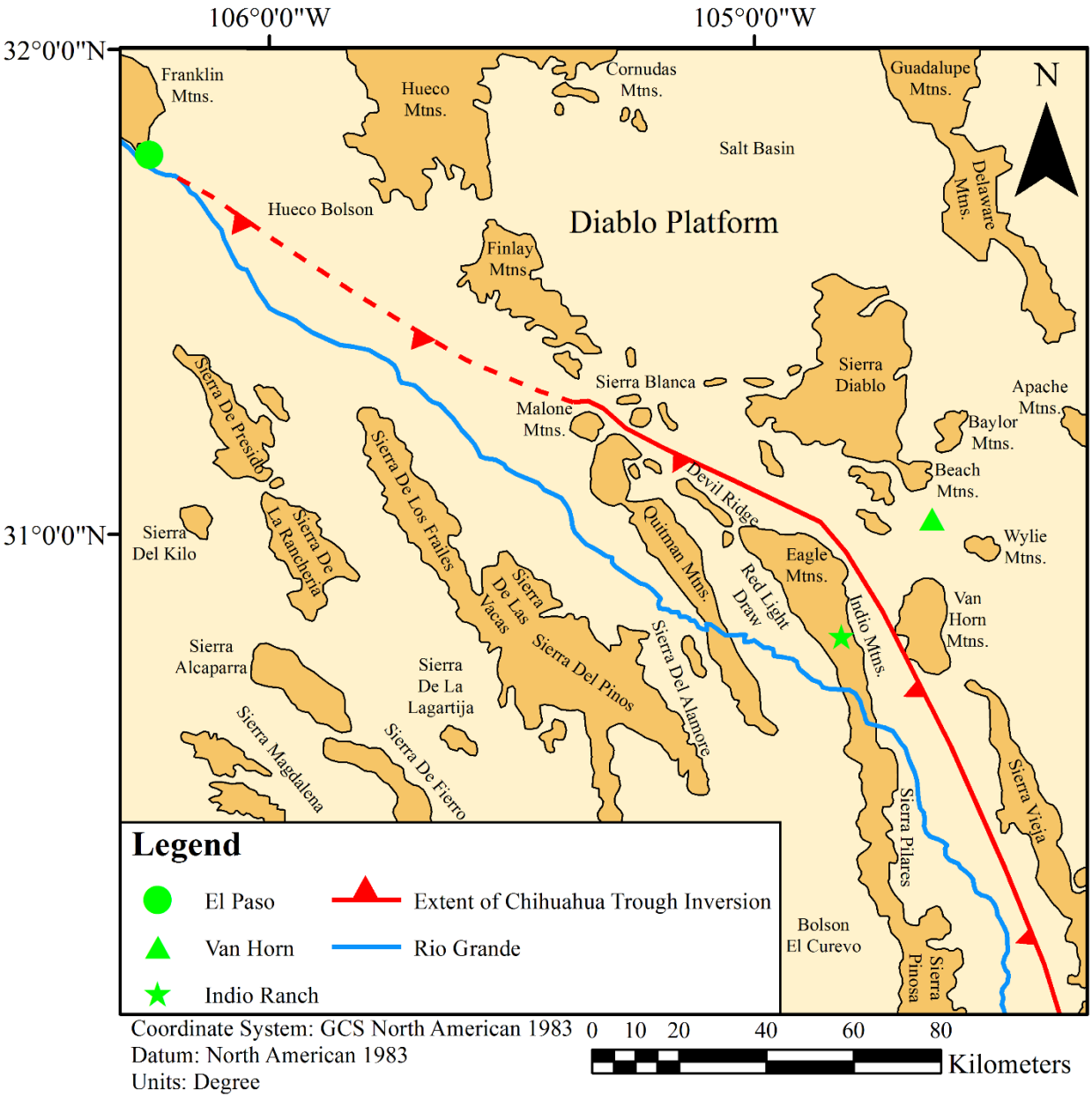

Figure 2: Eastern Chihuahua Trough Map
Eastern portion of the Chihuahua Trough with names of mountain ranges and locations of El Paso, TX, Van Horn, TX and the Indio Ranch. Modified after Underwood (1980), Rohrbaugh (2001) and Page (2011).

(Rohrbaugh, 2001; Carciumaru and Ortega, 2008) and due east in the northern region near Squaw Peak (Page, 2011). Rohrbaugh's and Page's findings are important because they illustrate heterogeneity in the Laramide inversion of the Chihuahua trough. These compressional faults led to folding. Detachment folds and drag folds combine to create complex, commonly overturned geometries in the foot wall of thrusts. These structures control the targets of this research. In addition to detachment folds and drag folds, broad-fault bend folds are present in an anticline-syncline pair found in the hanging wall of the Squaw Peak Thrust within the Yucca Formation (Page, 2011).

A third period of tectonic activity occurred in the Neogene with extensional processes associated with the Rio Grande Rift and the Basin and Range province affected the Indio Mountains by producing the Indio Fault (Rohrbaugh, 2001). The primary structure associated with this extension in the study area is the Indio Fault (Figure 3). Observed calcite-vein and growth-fiber orientations indicate a horizontal east-west extension direction and with simple fault modelling, a northwest-southeast striking normal fault is predicted with down-dip displacement (Rohrbaugh, 2001). However, the Indio Fault strikes northwest, with a shallow pitch and oblique slickensides, which indicate that dextral transtensional kinematics are required (Rohrbaugh, 2001) (Figure 3). In both the hanging wall and the foot wall of the Indio Fault, the Squaw Peak Thrust appears to be synfolded with the underlying Bluff Mesa unit, suggesting that the thrust occurred prior to these folds (Page, 2011). From the mapping of a previously unmapped imbricate thrust below the Bennett and Squaw Peak Thrusts, there is an estimated 1550 m of displacement (Page, 2011). Thus, the Indio Fault is responsible for exposing the easterly dipping units present today. There is a record of volcanic tuff along the East Ridge and the western margin of the Indio Fault Valley but not in the area of investigation (Rohrbaugh, 2001).

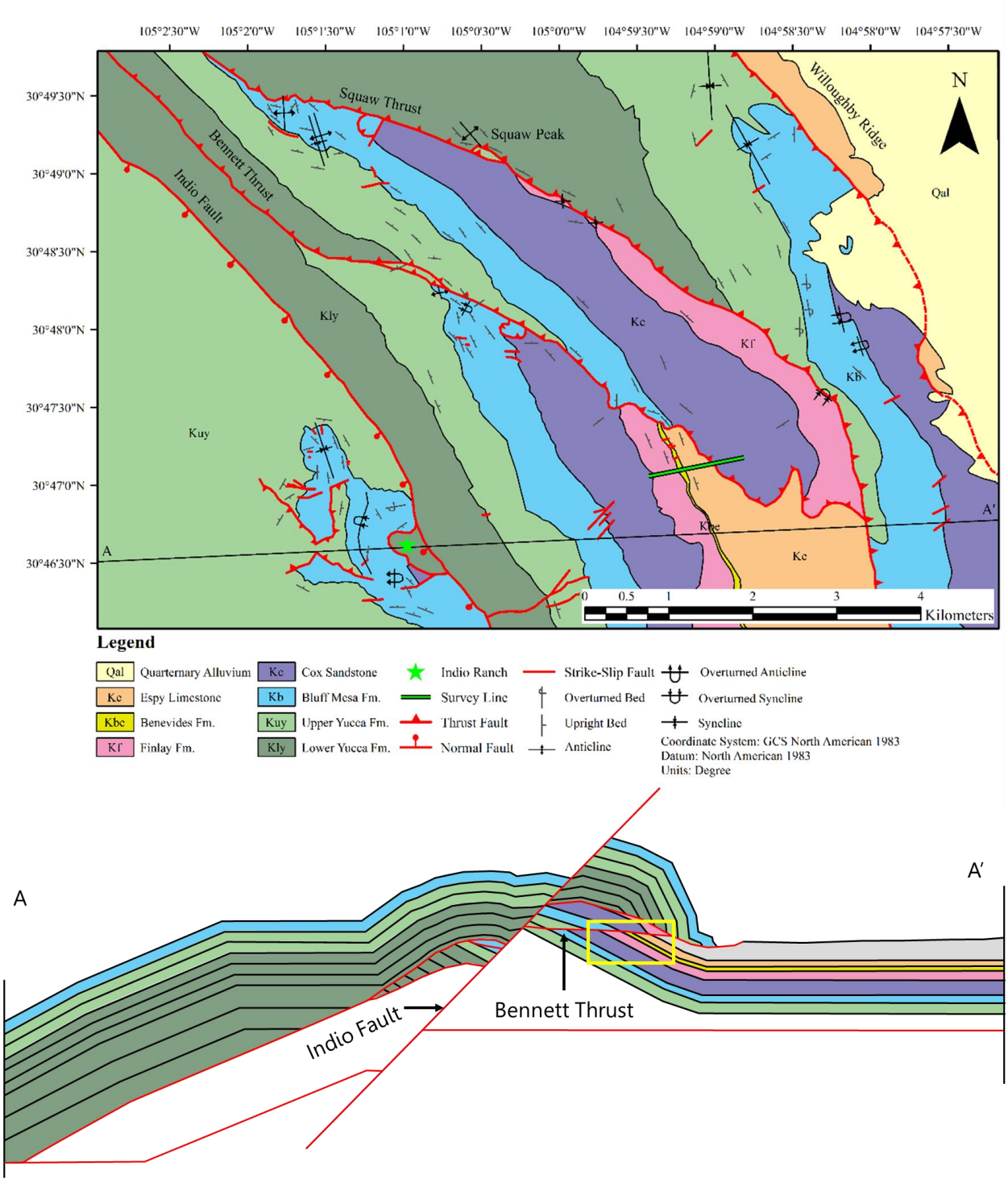

Figure 3: Indio Ranch Regional Map and Cross-Section
Top Panel: Geologic map of the central Indio Mountains displaying approximate survey geometry (green line) in relation to geologic units and structures. Bottom Panel: Structural reconstruction cross-section. Yellow box indicates approximate are on the cross-section imaged by the seismic reflection survey. Both panels are modified after Page (2011).

2.2 GEOLOGIC UNITS AND STRATIGRAPHY

In addition to modelling the subsurface structural features produced from extensional and contractional processes, this research aims to produce a model that delineates the interfaces between rock units, both exposed at the surface and contacts in the subsurface. The pre-rift rock units that are unexposed at the Indio Mountains are a Permian aged limestone lying unconformably on Precambrian metamorphic basement (King and Flawn, 1953; Underwood, 1980).

The exposed rock units in the Indio Mountains records the transgressive sequence of the Chihuahua Trough during the Cretaceous Period of the Mesozoic and are the only rock units included in the stratigraphic column (Figure 4). Rock units in the study area average a dip of 20° to 30° northeast (Langford and Pavlis; Rohrbaugh, 2001). The rock units are listed below, starting with the oldest first (Page, 2011; Rohrbaugh, 2001; Underwood, 1980).

Powwow Conglomerate Member and Hueco Limestone

Both of these units cropout in small exposures on the north flank of the Eagle Mountains. They record a transgressive sequence from the Permian sea onto the Diablo Platform. The trace fossils in the Hueco Limestone of the Eagle Mountains correlate to the same unit in the Hueco Mountains, approximately 60 km east of the Franklin Mountains in El Paso, TX (Underwood, 1980; King and Flawn, 1953).

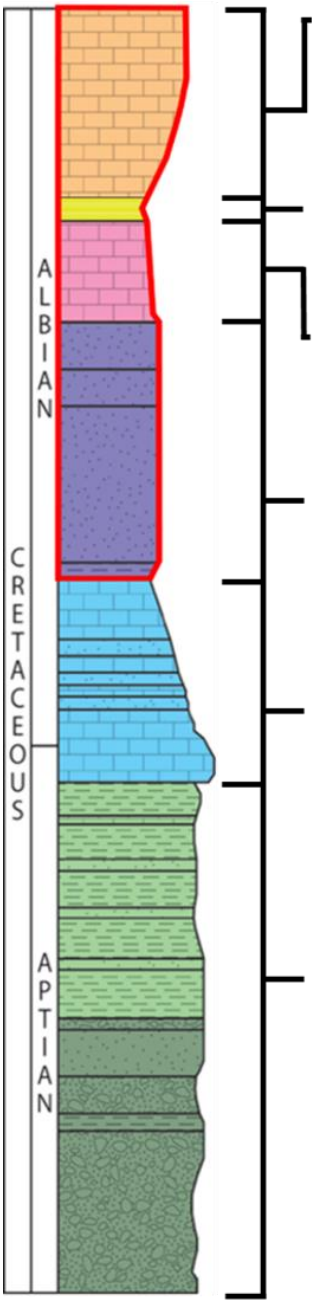

Espy Limestone

The Espy Limestone is composed predominantly of medium to dark-gray limestone. The lower section is characterized by shale with interbedded nodular limestone and marl. Fossils are predominantly bivalves with a small amount of gastropods. Fossils are abundant in the lower section and diminish in meter scale beds of the upper section.

Benevides Formation

Visible outcrops of the Benevides are usually limited to the orange-brown sandstone in the upper unit. The lower section is non-resistant, shaley siltstone. The upper exposed portions are characterized by their cross-bedding and intersecting fossilized burrows.

Finlay Formation

The Finlay Formation is a fine-crystalline, gray limestone consisting of massive beds 1-3 m thick. The Finlay formation is composed of dense fissil hash and identifiable gastropds and bivalves. Abundant silicified pelycpod shells on the jagged and weathered exposures are common.

Cox Sandstone

The Cox Sandstone is a cross-bedded, fine to medium grained, quartz arenite. The sandstone is fairly resistant to weathering and is a ridge former. Pale yellow to white sandstone mixed with iron-oxide stained grains is characteristic. Several lenses of conglomerate-sandstone composed of rounded quartz, chert and limestone exist but are not pervasive. Dark red shale units exist in the lower part of the unit. A 3 m thick, light gray fossiliferous limestone is present.

Bluff Mesa Formation

The Bluff Mesa is a fossiliferous, fine-grained to crystalline, gray limestone interbedded with quartz arenite and can be divided into 3 units. The lower section contains massive beds (up to 3 m) of fossiliferous limestone. Oolite rich beds are most abundant in this lower unit. The middle section consits of limestone beds 2 m or less in thickness. The limestone beds are interbedded by layers of quartz-arenite sandstone of a half meter or less in thickness and closely resemble the overlying Cox formation. The upper section consists of a fossiliferous, nodular, micritic limestone and is typically a valley former.

Yucca Formation

The Yucca formation can be divided into distinct upper and lower units. The lower unit is a conglomerate with clasts composed of gray limestone and black, pink and white chert cemented by a fine-grained maroon sandstone matrix. The clasts range from a few millimeters to approximately 20 cm in size.

A sudden fining upward sequence of sandstone in the Yucca defines the base of the upper unit, which consists of sandstone, shale, siltstone and limestone. The maroon shale layers are easily eroded and define slopes with an average thickness of 1 to 2 m. The siltstone is typically dark brown with an average thickness less than 1 meter. 2 limestone layers are in the upper portion of the Yucca column. The lower limestone bed averages 3 meters in thickness and the upper bed marks the Yucca-Bluff Mesa contact

Figure 4: Stratigraphic Column

Generalized stratigraphic column of geologic units present in the Indio Mountains. Red line indicates which units are encompassed by the survey and color of geologic units correspond with those in Figure 3. Modified after Underwood (1980) Rohrbaugh (2001) and Page (2011).

Yucca Formation

The Yucca Formation is the lowest rock unit exposed in the Indio Mountains. A section 610 m thick is exposed in the footwall of the Indio Fault, but this is a minimum thickness could extend deeper into the subsurface. The Yucca Formation can be divided into two units (Page, 2011; Li, 2014; Fox, 2016). The lower unit is composed of conglomerate with limestone and chert clasts in a maroon matrix. Clasts range from sand to cobble sized and are interbedded with small beds of sandstone and shale. The upper unit is composed of interbedded gray/white and red/brown sandstones and siltstones, maroon shales, nodular limestones, and two fossiliferous limestone layers in the uppermost 60 m. The source for the conglomerate clasts is primarily from the Permian, composed of interbedded limestone and quartz arenite, with chert intervals that form the clasts in the Cretaceous rocks. The upper unit is composed of interbedded gray/white and red/brown sandstones and siltstones, maroon shales, nodular limestones, and two fossiliferous limestone layers in uppermost 60 meters. The source rock is the same as the Permian aged Powwow Conglomerate: the Diablo Platform to the east (Underwood, 1980; Rohrbaugh, 2001; Page, 2011; Li, 2014; Fox, 2016).

Bluff Mesa Formation

The Bluff Mesa Formation is a carbonate unit with a thickness of 242 m in the footwall of the Indio Fault (Page, 2011; Li, 2014; Fox, 2016). The Bluff Mesa Formation can be divided into three units. The lower unit is composed of a 3 m thick massive fossiliferous limestone that is oolite rich. The middle unit is fossiliferous, nodular, micritic limestone and typically forms valleys. The upper unit is composed of fossiliferous, nodular, micritic limestone and are typically forms valleys. Orbitolina is an index fossil found only in this formation in the region (Underwood, 1980; Rohrbaugh, 2001; Page, 2011; Li, 2014; Fox, 2016).

Cox Sandstone

The Cox Sandstone is exposed 365 m in the footwall of the Indio Fault and is composed of well-cemented quartz arenite with interbedded red shales at the base. Pebble conglomerates are sporadically found and two thin beds of fossiliferous limestone occur at top of the formation (Underwood, 1980; Rohrbaugh, 2001; Page, 2011; Li, 2014; Fox, 2016).

Finlay Formation

The Finlay Formation is 244 m thick in the Indio Mountains and is composed of massive, fine-crystalline, gray limestone beds (Page, 2011). Trace fossils include dense fossil hash, gastropods, bivalves, and pelecypod shells (Underwood, 1980; Rohrbaugh, 2001; Page, 2011; Li, 2014; Fox, 2016).

Benevides Formation

The Benevides Formation is exposed 30 m thick in the study area and can be divided into two units. The lower unit is a shaley-silt stone and the upper unit is and orange-brown sandstone that is cross-bedded and has burrow trace fossils (Underwood, 1980; Rohrbaugh, 2001; Page, 2011; Li, 2014; Fox, 2016).

Espy Limestone

The Espy Limestone can be divided into two units. The lower unit is composed of interbedded shale and marl, with bivalve and gastropod fossils. The upper is predominantly medium/dark grey limestone (Underwood, 1980; Rohrbaugh, 2001; Page, 2011; Li, 2014; Fox, 2016).

3. Field Methods and Data Acquisition

Table 1 describes the survey geometry and information for the seismic line over the Bennett Thrust Fault. The survey line exploited the access road to the Indio Ranch field station, with shots and receivers placed off the road in a linear array (Figure 6). Three GPS base stations, TOPCON GB-1000 receivers and PG-A1 antennas with ground planes, were used to survey the benchmark locations using static measurements. The base stations were left in the field for two hours with antennas set over benchmarks to ensure precision. All base station locations were surveyed one week prior to surveying shot and receiver locations. Real Time Kinematic (RTK) surveying used GPS and GLOSSNASS satellite constellations. TOPCON GR-3 base-station and rover were used when surveying the shot and receiver locations. This precise and accurate surveying technique was necessary for the short and dense geometry of this survey.

Table 1: Field Methods and Data Acquisition Parameters

Survey Line Length	1.0 km
Number of Receivers and Data Recorders	200
Receiver Spacing	5.0 m
Receiver Frequency	4.5 Hz
Receiver Sampling Rate	2.0 ms
Number of Sources	100
Source Spacing	10 m
Source Depth	0.5-1.0 m
Explosive Source Weight	150 g
Number of 3.5 kg Hammer Sources	490

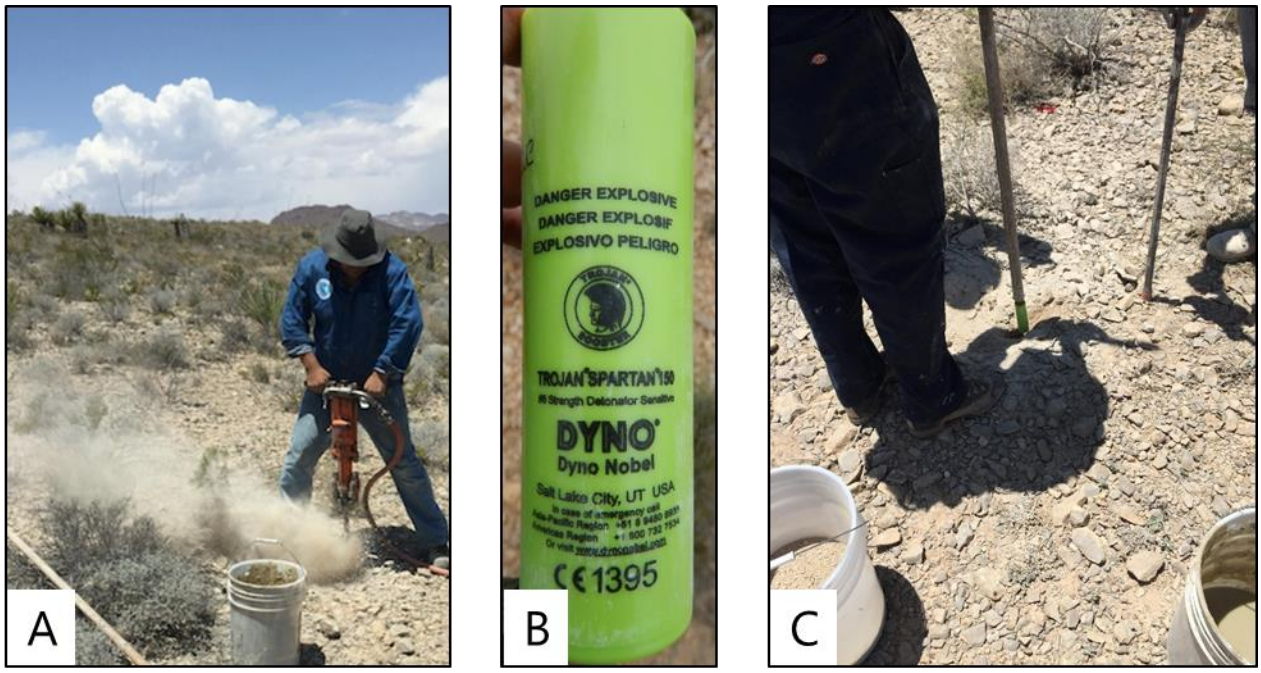

Figure 5: Shot Deployment Images
A: Student drilling shot hole with air-powered rock drill. B: 150 gram Dyno Nobel Trojan Cast Booster. C: Shot placement.

Sources are placed 0.5-1.0 m in the ground (Figure 5). On either end of the survey line, five Dyno Nobel Trojan Cast Boosters were detonated and one Dyno Nobel Trojan Cast Booster was detonated along the line (Figure 5), with the exception of shot point 135, indicated by the red circle on the lower map in Figure 6; at the time of shot deployment, shot 135 was unable to be detonated due to unsuitable conditions. Five 3.5 kg sledgehammer blows were recorded at each shot point, with the exception of shot points on either end of the line and shot point 135. There is little to no topsoil in this area, so an air-powered rock drill was required to drill to the appropriate depth (Figure 5). While it is common practice to orient survey lines perpendicular to the strike of a given target, in this case the Bennett Thrust Fault, an exception was made in this survey. The orientation of the survey line is slightly oblique to the strike of the fault because the air-powered rock drill used to place shots at designated locations was connected to a large air-compressor hitched to the back of a vehicle by 300 feet of hose. There was not enough length of hose to reach

locations of shots that would make the line perpendicular. Special considerations had to be taken into account at the time of shot and receiver deployment if the location for either were in the middle of the road; deployment locations were shifted inline to avoid being deployed in the road. Additionally, it is common practice to orient the middle of a geophysical survey directly over the area of interest. However, this was unable to be done because the UTEP Field Station does not own the property to the northeast of the orange colored line pictured in Figure 6.

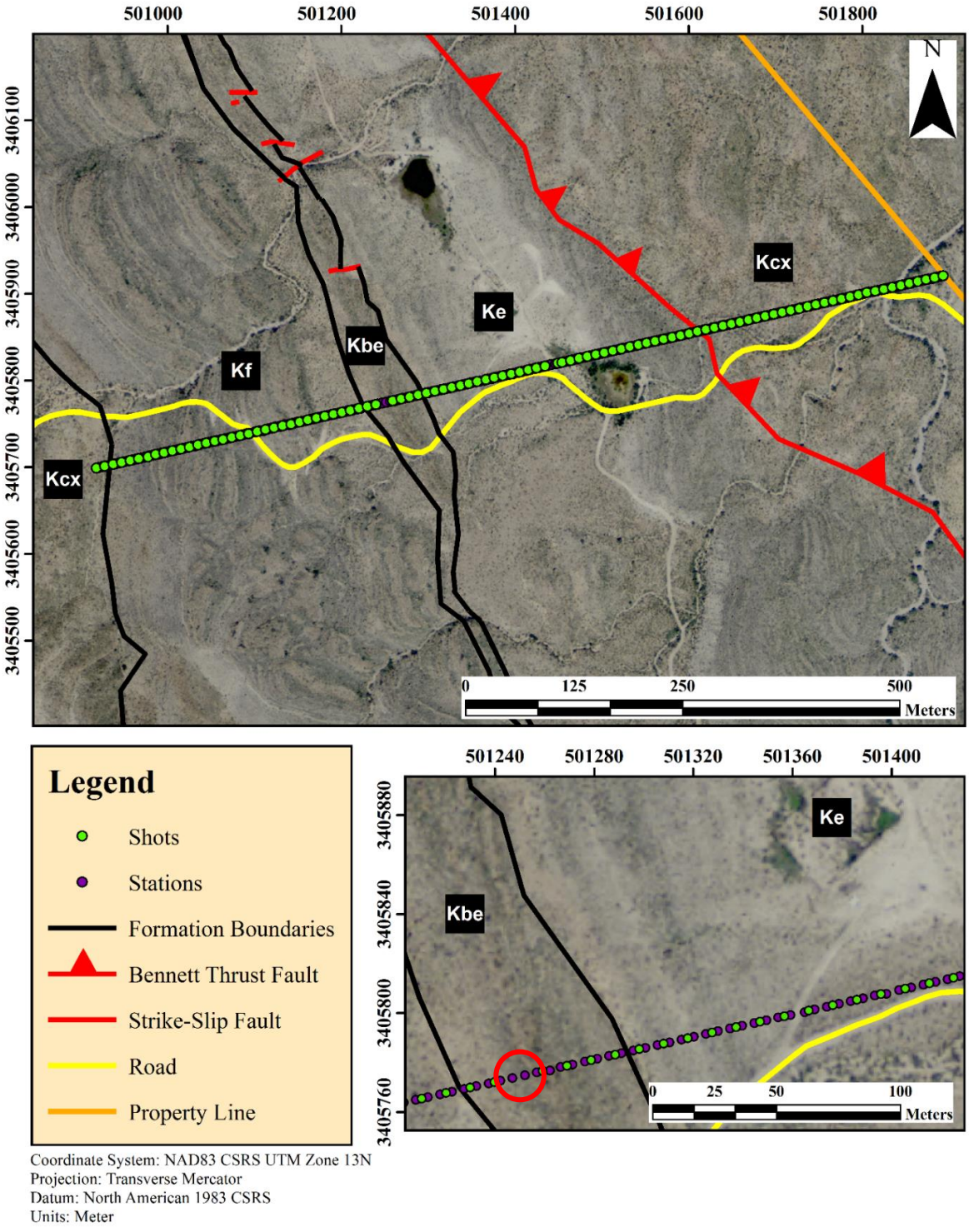

Figure 6: Survey Map
Maps displaying survey geometry in relation to geologic formations and structural features. Black circle indicates location of undeployed shot. Kcx defines Cox Sandstone, Kf defines Finlay Formation, Kbe defines Benevides Formation, Ke defines Espy Limestone.

4. Reflection Processing Methods

The goal of the seismic reflection technique is to quantify the time taken for a seismic wave, in this case the P wave, to travel from a source, at a known location, reflect of a boundary in the subsurface, and then travel back to the surface where it is recorded by a by a receiver, at a known location (Reynolds, 2011; Waters, 1987). The reflection method not only models the geometry of the structures in the subsurface, but also the physical properties of the lithological units present (Reynolds, 2011; Waters, 1987). In order to do so, a number of steps, processes and operators must be implemented in a particular order, referred to as a seismic processing flow (Figure 7). I will layout the flow used to process both datasets in this study in the following sections, define each one, and state the parameters used in each step, process and operator.

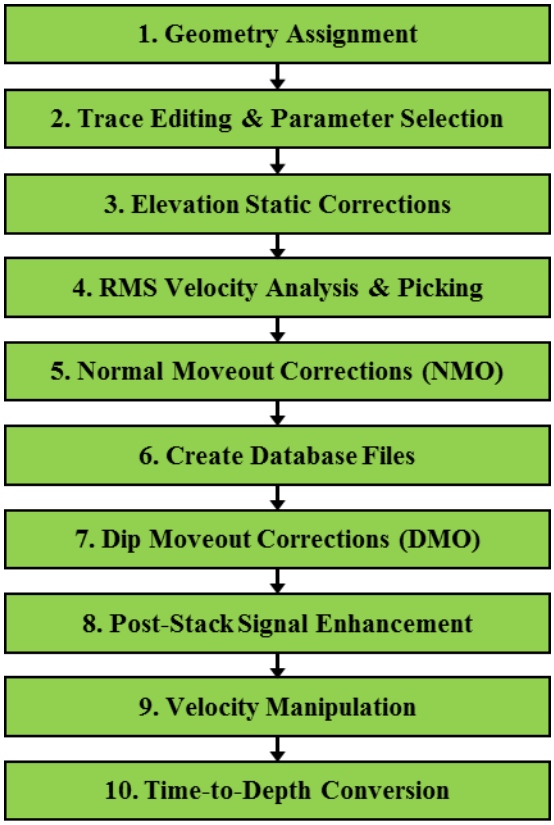

Figure 7: Reflection Processing Flow

4.1 GEOMETRY ASSIGNMENT

Geometry assignment is the first step in seismic processing. Without a correctly defined survey geometry, subsequent processing techniques will not operate as they should. Geometry assignment can be quite complicated and tedious, depending on the symmetry and design of the survey. However, the survey geometry in this study is very simple, straight and symmetrical. Figure 6 displays shot and receiver locations of the survey. Geometry is assigned using the 2D land Geometry Spreadsheet process (Figure 8). There are 4 operators within this process: Geometry Setup, Receiver Setup, Sources Setup and Land 2D Binning.

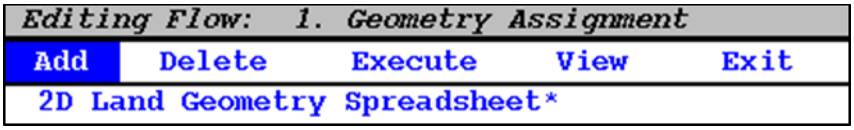

Figure 8: Geometry Assignment Flow
Flow outlining the 2D Land Geometry Spreadsheet used for geometry assignment. Screenshot from ProMAX

Geometry Setup requires the receiver-station interval, the source-station interval, the first and live station number, the source type, and length units used. The Receiver Setup requires X and Y coordinates and elevation of receivers. The Sources Setup requires X and Y coordinates and depth to which the shots are placed. Both the Receiver Setup and Sources Setup are able to populate appropriate values to the spreadsheet from an ASCII file containing the geometric data. The X and Y coordinates used are derived from the coordinate system and projection (Figure 5) and the units of elevation and depth to which the shots are placed are meters. Land 2D Binning calculates and assigns common depth points (CDP), calculates offset of shots and receivers and creates a database in which this information is stored and accessed for subsequent processing. This step in the processing flow is identical for both the high and low frequency datasets.

4.2 TRACE EDITING & PARAMETER SELECTION

Prior to further processing, editing and pre-processing measures must be applied to the raw shot gathers, such as muting noise, bad data, and bad traces, applying a deconvolution operator and filter.

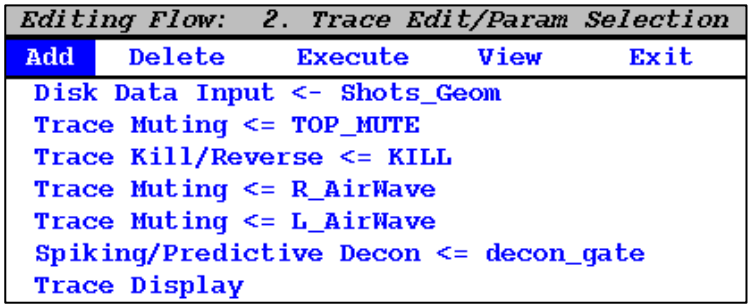

Figure 9: Trace Editing & Parameter Selection Flow
Flow outlining the trace editing and pre-processing measures used. Screenshot from ProMAX

4.2.1 Trace Muting

Trace muting is a valuable operator when editing and differentiating coherent signal from disruptive noise. It does this by setting all data affected by the mute operator to zero. Three trace mutes have been applied in the processing flow (Figure 9). TOP_MUTE is implemented to set all values above the mute gate to zero. Prior to the first arrivals, there is noise observed that could cause issue in further processing. R_AirWave and L_AirWave are surgical mutes. In this case, the surgical mutes are implemented to set the values between the mute gates to zero, accounting for the noisy airwave from the source. It is determined that this noise is the airwave by measuring the velocity of the feature, which measures to be 330 m/s (Campbell et al., 2010; Reynolds, 2011).

4.2.2 Trace Kill/Reverse

Trace killing removes completely noisy traces from a shot gather prior to processing. However, it is important to note that over-killing traces can be detrimental. Repeating noisy traces throughout shot gathers should be killed and removed from the data.

4.2.3 Spiking/Predictive Deconvolution and Bandpass Filtering

The objective of deconvolution is to estimate the effects of reverberation, attenuation, and ghosting, which are caused by the response of the signal with the geophones and the Earth itself (Burger et al., 2006; Reynolds, 2011). It is an analytical procedure used to remove the effects of previous natural filtering (Bekara and van der Baan, 2009; Reynolds, 2011). Dereverberation refers to the process by which ringing associated with multiple reflections is attenuated. Deghosting removes the effects of energy that leaves a source, travels upwards and is reflected back to the receiver. Ghosting is caused by signal bouncing off the water/air interface or the weathered layer (Baker, 1999; Reynolds, 2011).

The type of deconvolution applied is minimum phase predictive, which applies a traditional Wiener-Levinson predictive operator (Landmark; Treitel, 1974). After deconvolution is implemented, a single Ormsby bandpass filter is implemented, which applies a single filter to all traces at all times. The filter frequency values are determined from the spectral analysis of a raw shot gather (Figure 10). The bandpass filter applied to the explosive data is 5-10-15-30 (Hz), while the filter applied to the hammer data is 20-40-70-140 (Hz).

4.2.4 Raw Shot Gathers, Post Trace Editing, and Parameter Selection

Prior to trace editing and parameter selection, raw shot gathers (Figure 11) are noisy and incoherent in some places. The airwaves interfere with the coherent signal and the streaky traces need to be killed and removed from the shot gather.

After trace editing and parameter selection are applied by the flow and processes described above, the airwaves are filtered and muted. Noisy traces are killed, the recorded noise prior to the first arrivals is also removed and set to zero. Minimum phase predictive deconvolution removes all unwanted effects previously described and the Ormsby filter removes the unwanted frequencies. Figure 12 shows shot gathers are processed and are ready for subsequent processing. This same workflow is applied to the hammer dataset as well, using the same killed traces and top mute.

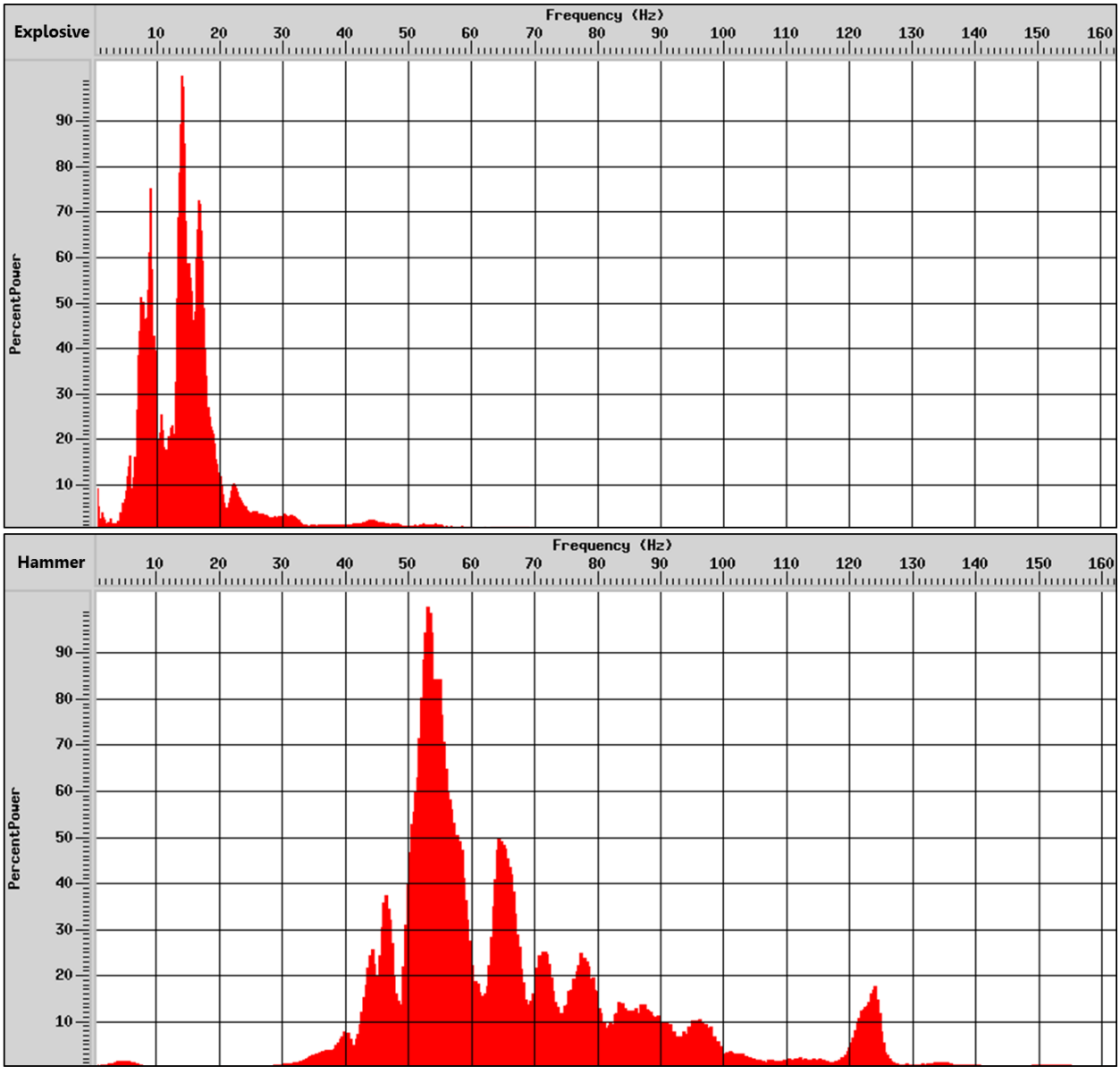

Figure 10: Frequency Spectra
Frequency spectra of raw explosive and hammer gathers at shot point 150. X-axis displays frequencies recorded in Hertz (Hz) and Y-axis displays percentage of dominant frequencies from each gather. Screenshots from ProMAX.

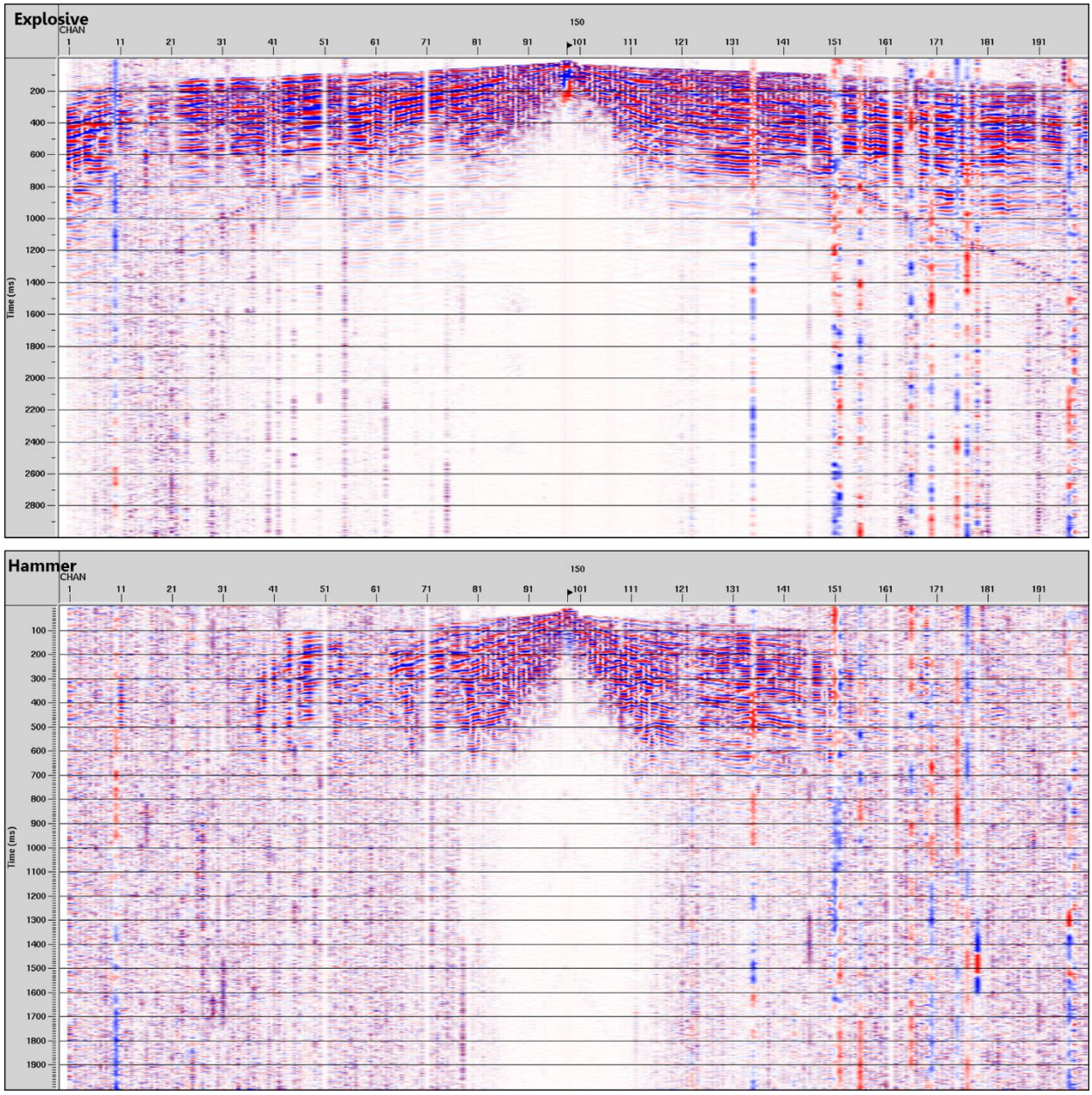

Figure 11: Raw Shot Gathers
Raw shot gather from explosive and hammer datasets prior to trace editing and parameter selection. Shot gather 150 with 5-meter receiver spacing and 10-meter source spacing. Screenshots from ProMAX.

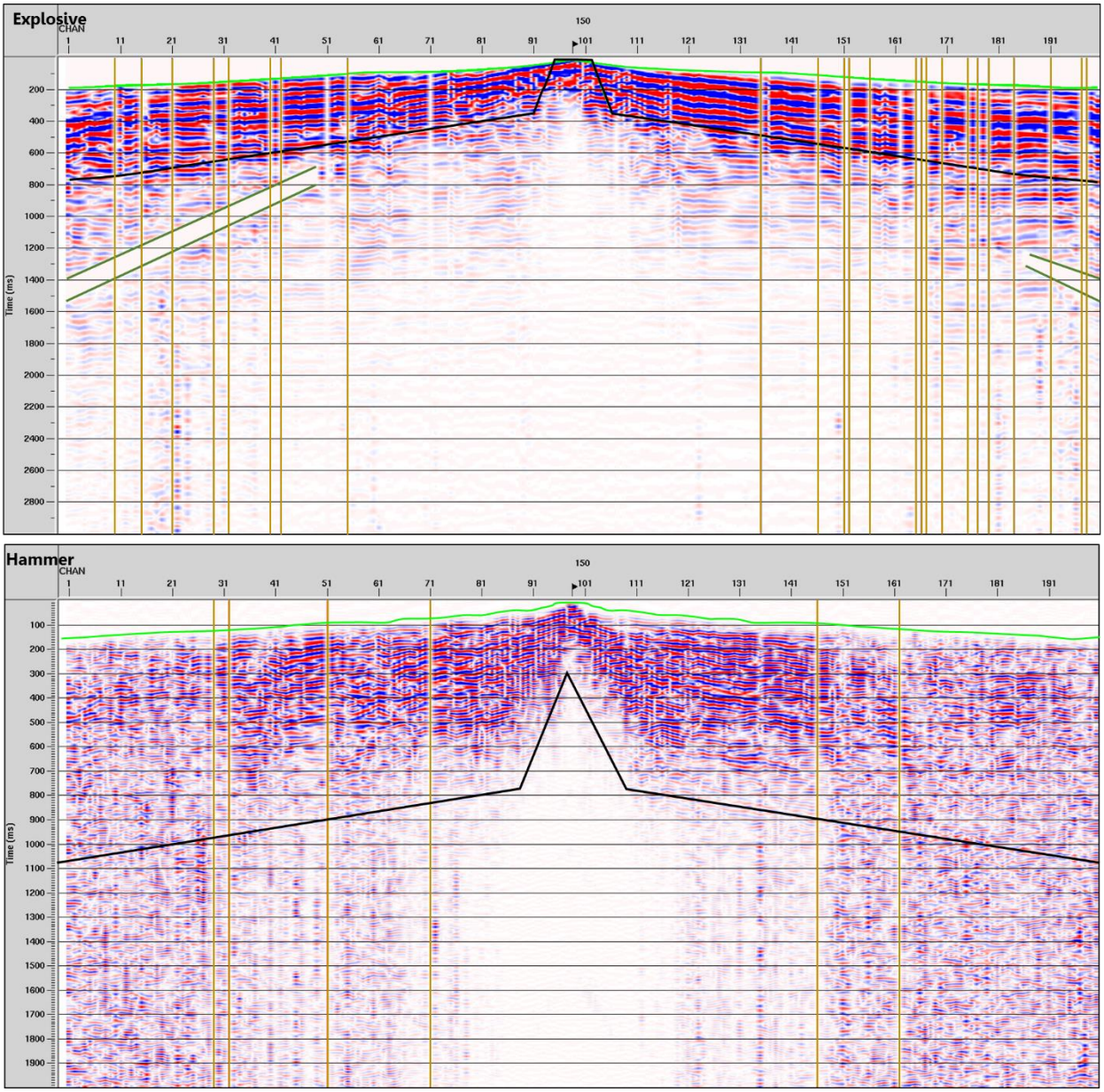

Figure 12: Pre-Processed Shot Gathers
Shot gather after trace editing and parameter selection is applied for explosive and hammer gathers. Vertical brown lines indicate killed traces, the lime green line indicates the TOP_MUTE gate, the black line indicates the deconvolution gate and the dark green lines indicate the airwave surgical mute. Shot gather 150 with 5-meter receiver spacing and 10-meter source spacing. Screenshots from ProMAX.

4.3 ELEVATION STATIC CORRECTIONS

The survey at the UTEP Field Station in the Indio Mountains was undertaken over rugged and irregular terrain; with a length of 1.0 km, there is an elevation change of nearly 100 m. Elevation static corrections account for the time shifts needed at the shot and receiver locations (Hunter et al., 1984; Reynolds, 2011). Elevation static corrections adjust traces to appear as though they were collected at the final datum elevation (Baker, 1999; Burger et al., 2006). The travel time taken from a reflector to a given geophone will be delayed by the difference in elevation divided by the seismic velocity of the near surface layer (Feroci et al., 2000; Reynolds, 2011). In order to correct for this delay, an average velocity is assigned to the area above the final datum. The following sections will describe the flow and processes involved in these corrections (Figure 13). The data input is sorted by the CDP header value for the next processing steps, and the same parameters in this step in the processing flow are identical in both the explosive and hammer datasets.

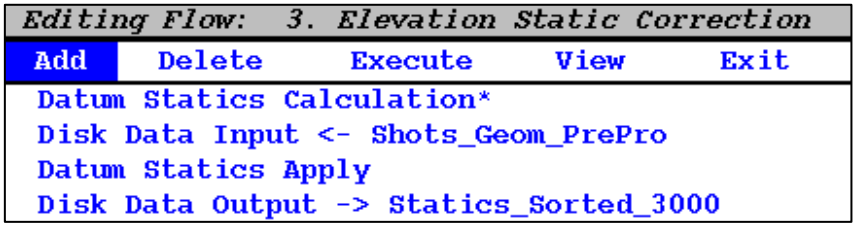

Figure 13: Elevation Static Corrections Flow
Flow outlining elevation static corrections. Screenshot from ProMAX.

4.3.1 Datum Statics Calculation

This operator is able to be used for both elevation and refraction static corrections but for this process, elevation static corrections is used (Figure 14). Elevation statics are computed to the final datum and calculates shot, receiver and CDP mean statics. The final datum elevation is determined by the lowest lying receiver elevation. The replacement velocity is tested against a number of velocities; replacement velocities of 2000 m/s, 3000 m/s and 4000 m/s are tested.

However, the difference in subsequent processing is negligible, therefore the mean of the tested replacement velocities is chosen for elevation static corrections.

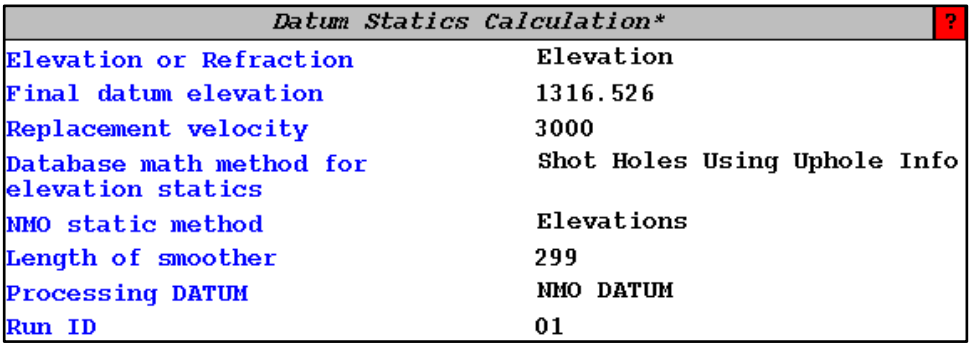

Figure 14: Datum Statics Calculation Process
Parameters used in the Datum Statics Calculation operator to be applied in elevation static corrections. Screenshot from ProMAX.

4.3.2 Datum Statics Apply

The Datum Statics Apply operator applies the values from the Datum Statics Calculation and reads three static values from the file database: a total source static file, a total receiver static file and a CDP mean static file. With these files, ProMAX computes and applies the static corrections prior to NMO. The dataset is then output to a new dataset with all of the processes and operators described (Figure 13).

4.4 VELOCITY ANALYSIS & PICKING

The most critical step in reflection processing is the determination of the seismic velocity of the lithological units under investigation (Waters, 1987; Reynolds, 2011). It is the factor which is used to convert from the time to depth domain (Feroci et al., 2000; Reynolds, 2011). The intention of velocity analysis is to be able to accurately pick the stacking (RMS) velocity for subsequent processing, NMO corrections and time to depth conversion (Burger et al., 2006; Reynolds, 2011). During the velocity analysis process, data is sorted into CDPs, velocities are picked in order to correct for NMO, and applied to a dataset output for further processing. Figure 15 outlines the flow used for this process for both the shot and hammer data.

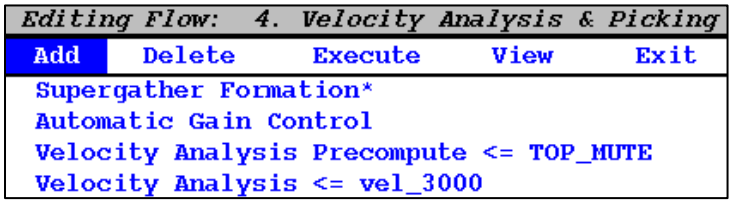

Figure 15: Elevation Static Corrections Flow
Flow used for velocity analysis and picking. Screenshot from ProMAX.

4.4.1 Supergather Formation

The Supergather Formation operator allows for easy formation of CDP supergathers. It specifies the location and range of CDPs packaged together into ensembles for Velocity Analysis (Figure 16). The Supergather Formation operator is a combination of the Disk Data Input and Ensemble Redefine operators (Landmark). Note, when acknowledging the warning "Warning >> This menu is obsolete. Please use the new 2D Supergather Formation tool." and attempting to use this suggested tool, ProMAX crashed. The dataset input is previously sorted by the CDP header from elevation static corrections flow (Figure 13). A CDP increment of 10 is initially used and later an increment of 5 is implemented to better constrain velocity picks.

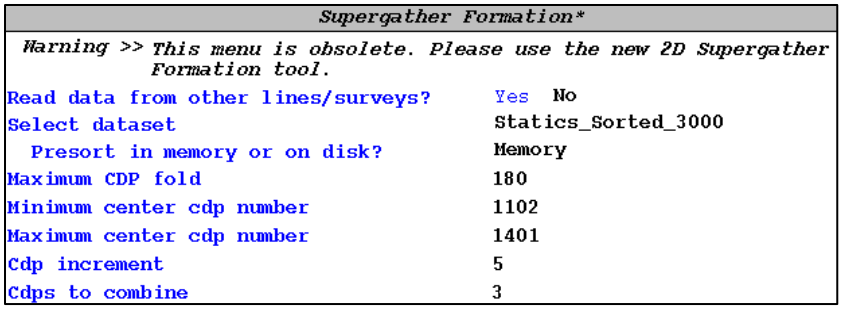

Figure 16: Supergather Formation Process
Parameters used in the Supergather Formation to be used in Velocity Analysis and to be applied in NMO corrections. Screenshot from ProMAX.

4.4.2 Automatic Gain Control (AGC)

An AGC operator is required to run the flow, otherwise the flow will crash. A default value of 500 is used.

4.4.3 Velocity Analysis Precompute

Velocity Analysis Precompute prepares the sorted data for input into Velocity Analysis by calculating the velocity spectral values, stacks CDP traces to create supergathers, and creates velocity function stacks at specified CDP locations (Landmark). Using the Velocity Analysis Precompute significantly speeds up the Velocity Analysis session (Landmark). Default parameters are used for all values excluding the minimum and maximum velocity semblance analysis values. These values correspond with the minimum and maximum velocity values in the velocity spectra panel in Figure 17.

4.4.4 Velocity Analysis

Figure 17 displays a sample Velocity Analysis panel, with the X axis displaying velocity in meters per second and the Y axis displaying time in milliseconds. The velocity spectra panel on the left displays the more common velocites from the CDP supergather with the warmer colors and the lesser common velocities in the cooler colors. The goal of Velocity Analysis is to be able to pick the velocities from the velocity spectra to match the values derived from the slopes of the features in the offset panel and prominent linear features in the Dyn (Dynamic) panel. These picks

are stored in a Stacking (RMS:Root Mean Square) Velocity table to be used in subsequent processing, such as NMO corrections and a time to depth conversion. Due to the faulted, folded and fractured nature of the Indio Mountains, velocity reversals are to be expected.

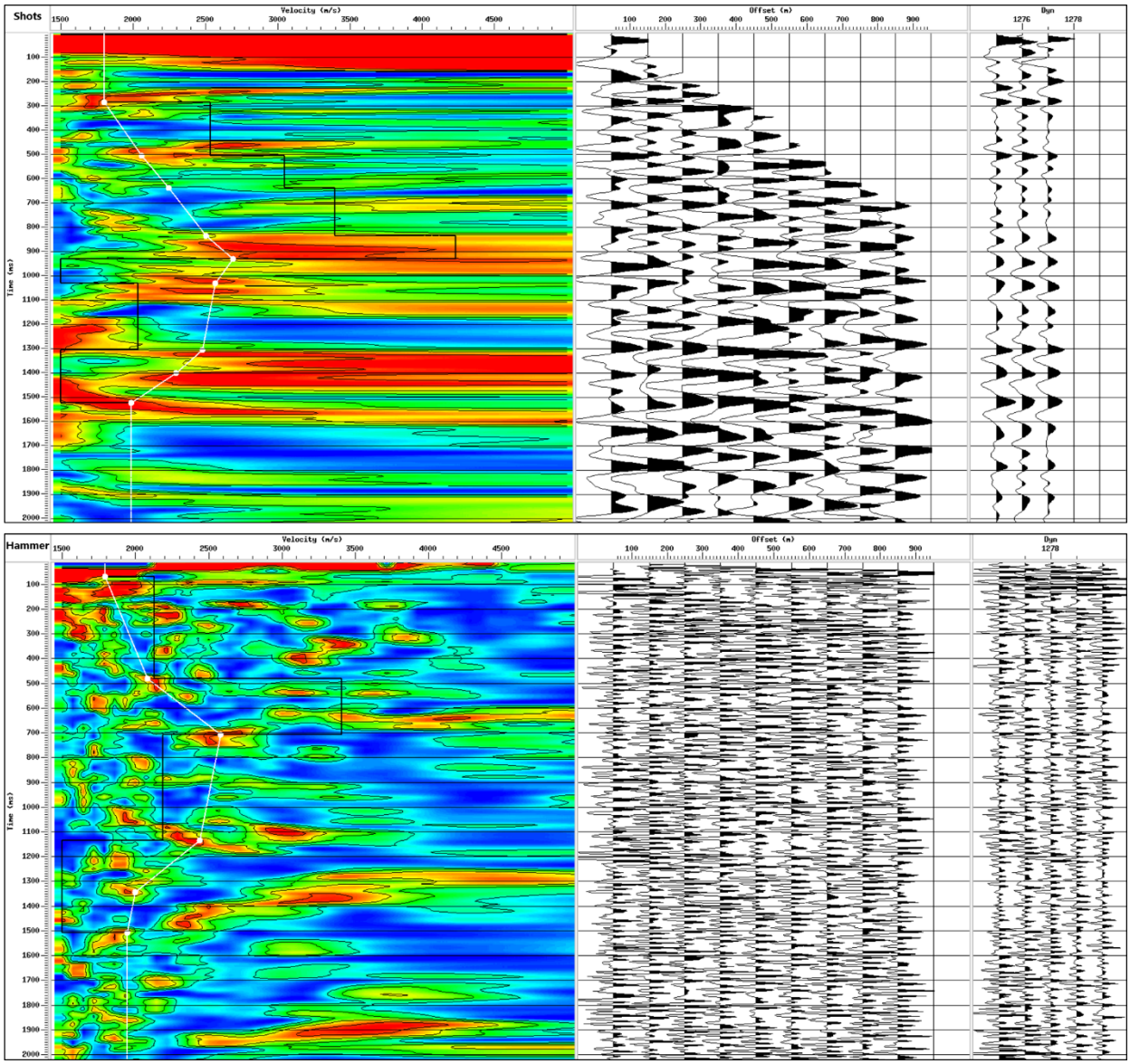

Figure 17: Velocity Spectra of Explosive Dataset
Supergather from CDP 1278 of explosive and hammer datasets. Velocity spectra with picked velocities, interval velocities, offset and Dyn panels. Screenshots from ProMAX.

4.5 NORMAL MOVEOUT CORRECTIONS (NMO)

NMO is defined by Figure 18. The larger the source-receiver offset, the greater the NMO correction will be (Castle, 1994; Reynolds, 2011). The greater the two-way travel time, with a corresponding increase in velocity (as velocity tends to increase with depth), the smaller the NMO correction will be at a given offset (Waters, 1987; Reynolds, 2011). The rate of increase in NMO correction with greater offset is hyperbolic, displaying a curved reflection on a CDP Supergather (Figure 17). The goal of NMO correcting is to flatten these hyperbolic reflections. This section will outline the flow, processes and operators used for correcting normal moveout in both the shot and hammer data (Figure 19).

$$T_x = \sqrt{\left[{T_o}^2 + \left(\frac{X}{V}\right)^2\right]}$$

Figure 18: NMO Equation
Equation for NMO, where T_x is equal to the actual reflection time of the seismic event due to NMO effects, T_o is equal to the zero offset reflection time of the seismic event, X is equal to the actual source-receiver offset distance, and V is equal to the NMO or stacking velocity for the seismic event (Castle, 1994).

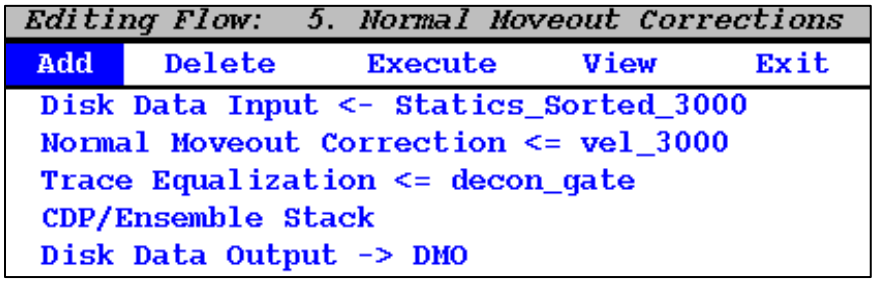

Figure 19: NMO Flow
Flow outlining processes and operators used in NMO. Screenshot from ProMAX.

4.5.1 Normal Moveout Corrections

Default parameters are used in the Normal Moveout Correction operator, along with the velocity table of picks, vel_3000, for corrections. Figure 20 shows four 1-D velocity models from the explosive dataset of select CDP locations along the survey line, picked during the Velocity Analysis and Picking step in the processing flow, at four lithological units in the area. These models further illustrate the heterogeneous nature of rock velocities in this study, due to the lithological characteristics of the rock units, along with the faulted, folded and fractured nature of present in the region.

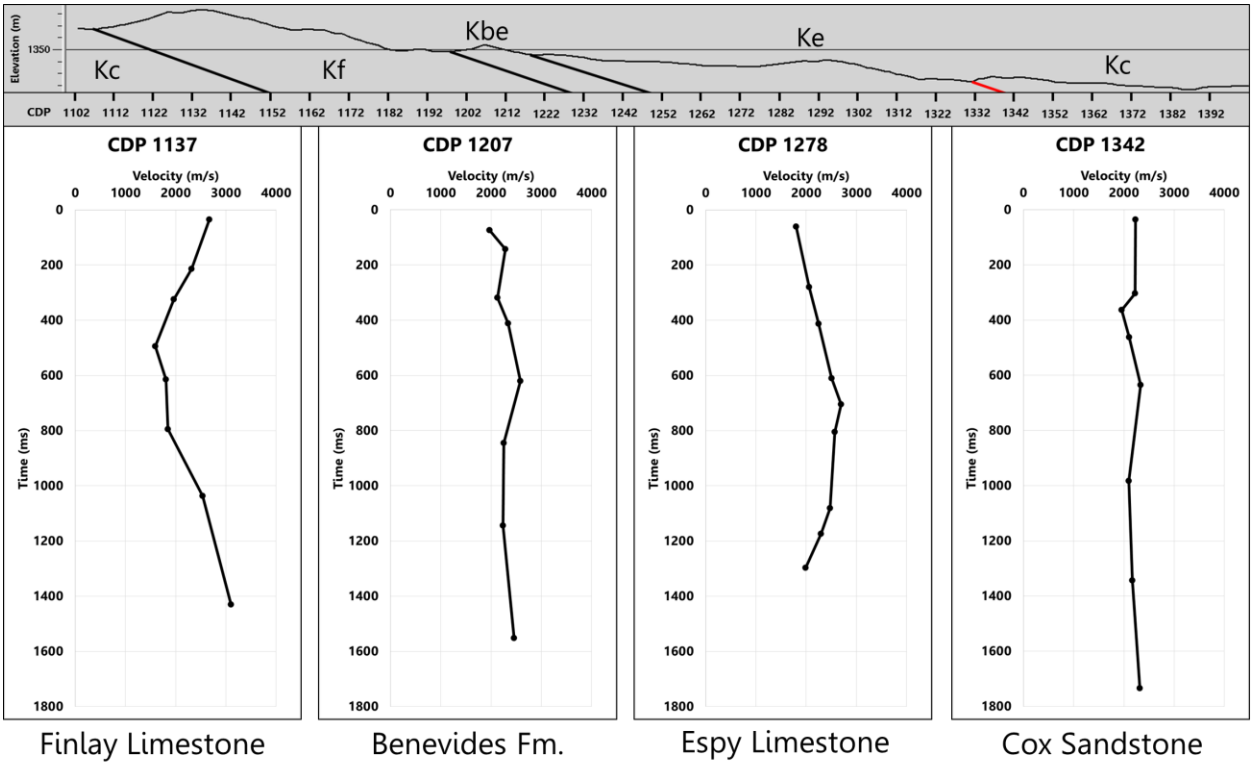

Figure 20: 1-D Velocity Models
1-D velocity models from select CDP locations along survey line with topographic profile, approximate dip lithological and fault contacts.

4.5.2 Trace Equalization

Default parameters are used in the Trace Equalization operator, along with the time gate parameter file, decon_gate, for calculations. Trace Equalization computes and applies a trace-to-

trace amplitude balancing function by using a single time window gate for each trace and the maximum amplitude of all traces. The object of this operator is to reduce variations in amplitude between traces to provide a closely clustered dataset available for subsequent processing.

4.5.3 CDP/Ensemble Stack

Once the NMO operator is processed (Figure 19), the dataset is output to an unstacked dataset, sorted primarily by the CDP bin number and input to the CDP/Ensemble stack operator to produce a stack ready for structural and lithological interpretation (Figure 21).

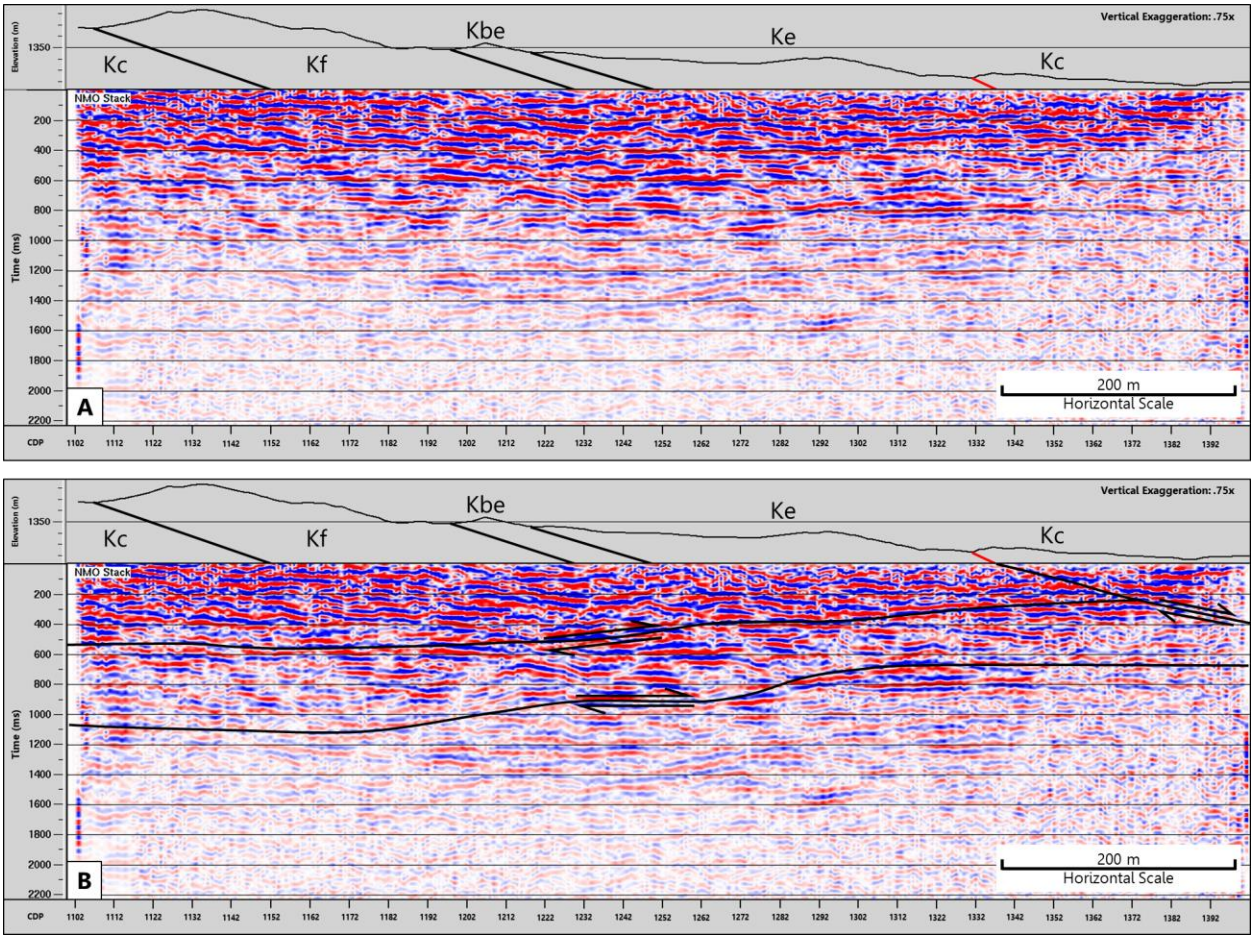

Figure 21: NMO Ensemble Stack
Explosive dataset NMO ensemble stack with topographic profile, approximate dip and lithological contacts labeled and indicated by black lines. Kcx defines Cox Sandstone, Kf defines Finlay Formation, Kbe defines Benevides Formation, Ke defines Espy Limestone. Panel A: Uninterpreted stack. Panel B: Interpreted stack, where red and black contact indicates Bennett

Thrust Fault in northeast part of stack and black lines indicate deeper faulting. Screenshots from ProMAX.

4.5.4 Disk Data Output

The data is then output to a new data set named DMO for further processing. Note, that the CDP/Ensemble Stack operator is disabled in the output to DMO, it is used here to gain a preliminary image of the stacked section (Figure 21).

4.6 CREATE DATABASE FILES

As the seventh process in the processing flow, DMO corrections, was attempted to be implemented, an error occurred which stated that the geometry and trace header values do not match the database; as the dataset is processed, some files may be lost, damaged or be incomplete.

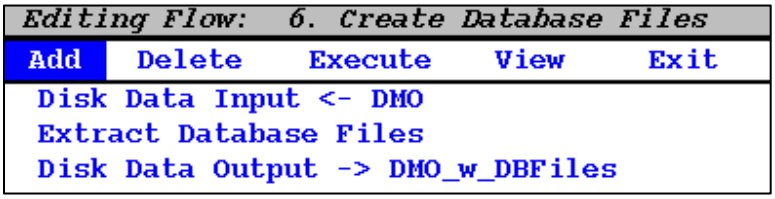

Figure 22: Create Database Files Flow
Flow used to update database with geometry and traceheader values. Screenshot from ProMAX.

In order to fix this error, Figure 22 outlines the flow used. The Extract Database Files operator (Figure 23) selects which information is extracted from the database and written to a new dataset. A new dataset is output for subsequent processing.

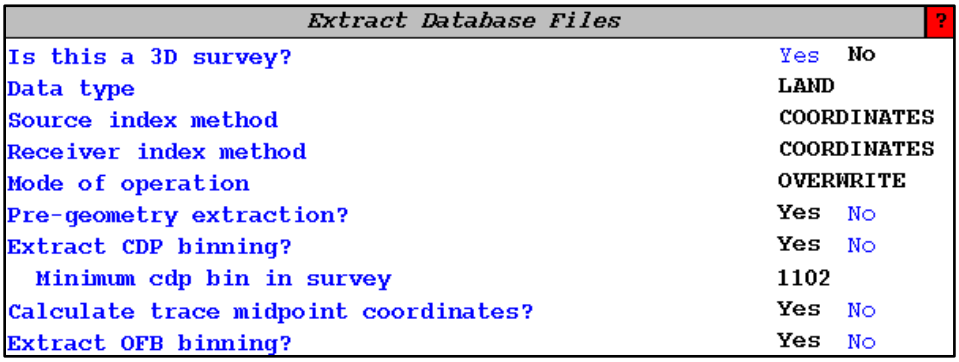

Figure 23: Extract Database Files Process
Parameters used in the Extract Database Files operator to be applied in the Create Database Files process. Screenshot from ProMAX.

4.7 DIP MOVEOUT CORRECTIONS (DMO)

Dip moveout corrections attempt to correct pre-stack data so shot gathers stack correctly, despite the dip of the lithological units (Deregowski, 1986; Reynolds, 2011). DMO corrections greatly improve velocity calculation, migration of dipping reflectors and noise reduction (Landmark, 1998). It is a pre-stack migration process which transforms the pre-stack data set so that each common midpoint (CMP) on the surface matches the CDP in the subsurface (Deregowski, 1986). DMO corrections combined with NMO corrections defines the complete mapping required to transform a finite-offset section to a zero-offset section (Deregowski, 1986; Reynolds, 2011). It ensures that pre-stack data velocities are not dip-dependent (Deregowski, 1986). This section will outline the flow used for DMO corrections (Figure 24). Processes involve trace header editing, binning DMO offset and applying those header edits and binning operators.

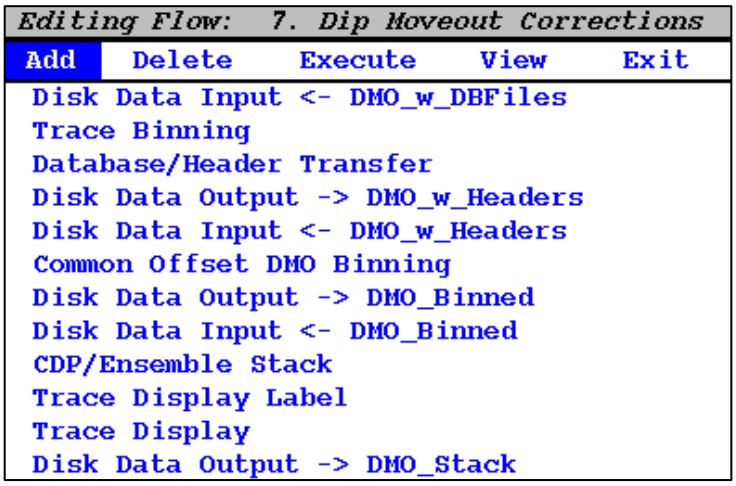

Figure 24: Dip Moveout Corrections Flow
Flow outlining the processes and operators used for DMO corrections. Screenshot from ProMAX.

4.7.1 Trace Binning

Trace Binning requires the initial disk data input's primary sort header to be the CDP bin number and the secondary sort header to be the absolute value of offset (Figure 26). Those absolute offset values are then transferred to the new DMO offset header values with the Trace Binning operator (Figure 26). Header entry bin centers and binned header entry values are the same values. They are determined by the offset on the first and last traces of the initial shot gather, 2.5-997.5, followed by the shot interval, 10. OFFSET and AOFFSET headers are set to bin center in order for the Common Offset DMO Binning operator (Figure 27) to operate. The following Database/Header Transfer then writes the DMOOFF header to the database with appropriate database files. Once Trace Binning and Database/Header Transfer complete, the dataset is output to a new dataset for subsequent processing.

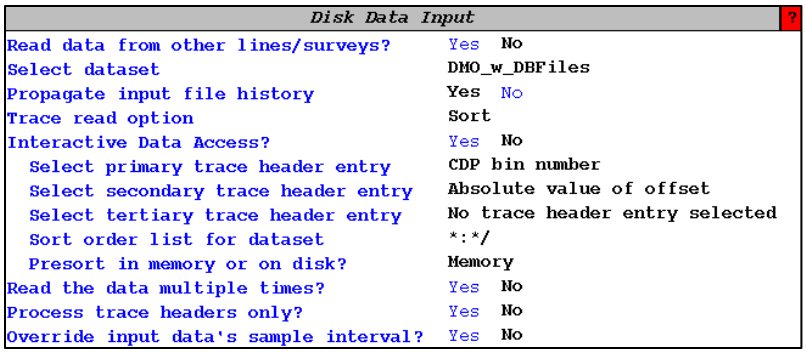

Figure 25: DMO Trace Binning Disk Data Input Process
Parameters used in the Disk Data Input operator to be applied in Trace Binning. Screenshot from ProMAX.

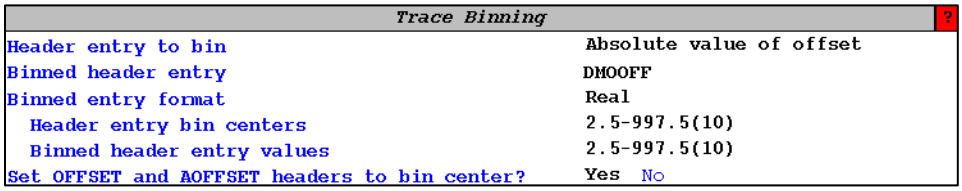

Figure 26: Trace Binning Process
Parameters used in the Trace Binning operator to be applied in DMO corrections. Screenshot from ProMAX.

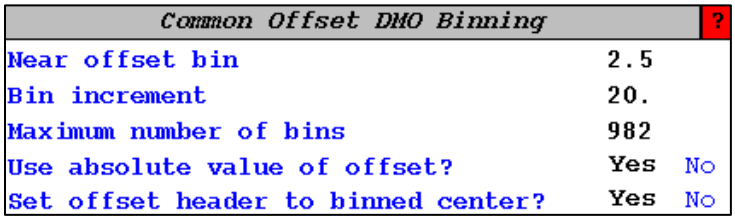

Figure 27: Common Offset DMO Binning Process
Parameters used in the Common Offset DMO Binning operator to be applied in DMO corrections. Screenshot from ProMAX

4.7.2 Common Offset DMO Binning

Common Offset DMO Binning requires disk data input's primary sort header to be the Offset bin for DMO and the secondary sort header to be the CDP bin number. The near offset bin value is determined by the distance to the center of the nearest DMO offset bin, which is the same value as the first offset value in Figure 27. It is necessary to have each common-offset section fully populated with a live trace at every CDP location. To ensure this is achieved, it is necessary to set the bin increment to twice the shot interval (Landmark). The maximum number of bins is simply calculated by Figure 28 (Landmark).

$$DMOOFF_{max} = OFF_{near} + (BIN_{total} - 1) * BIN_{inc}$$

Figure 28: Maximum DMO Offset Equation
Equation for maximum DMO offset, where $DMOOFF_{max}$ is equal to the maximum DMO offset, OFF_{near} is equal to the Near offset bin, BIN_{total} is equal to the total number of bins, and BIN_{inc} is equal to the bin increment.

4.7.3 CDP/Ensemble Stack

Once the Common Offset DMO Binning operator is processed (Figure 28), the dataset is output to an unstacked dataset, sorted primarily by the CDP bin number and input to the CDP/Ensemble stack operator to produce a stack ready for structural and lithological interpretation (Figure 29).

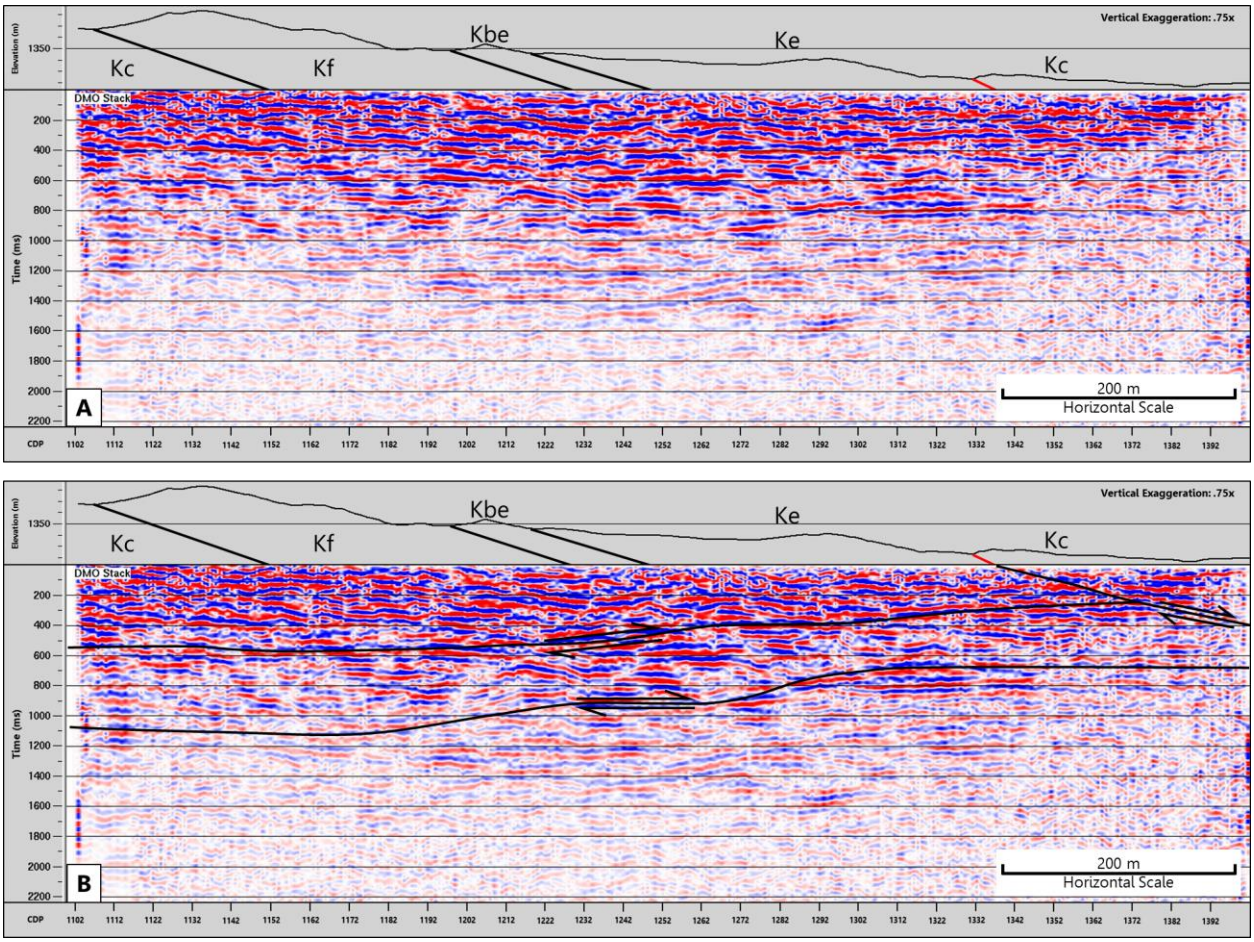

Figure 29: DMO Ensemble Stack

Explosive dataset DMO ensemble stack with topographic profile, approximate dip and lithological contacts labeled and indicated by black lines. Kcx defines Cox Sandstone, Kf defines Finlay Formation, Kbe defines Benevides Formation, Ke defines Espy Limestone. Panel A: Uninterpreted stack. Panel B: Interpreted stack, where red and black contact indicates Bennett Thrust Fault in northeast part of the stack and black lines indicate deeper faulting. Screenshots from ProMAX.

4.8 POST-STACK SIGNAL ENHANCEMENT

To further clean and optimize the stacked image (Figure 29), post-stack signal enhancement is often used and is successful in this study (Landmark, 1998). Three filters and techniques are implemented and visually compared to determine the optimal filtering procedure (Figure 30). IF/ELSE statements are implemented to reproduce traces and compare the three filters in the same screen.

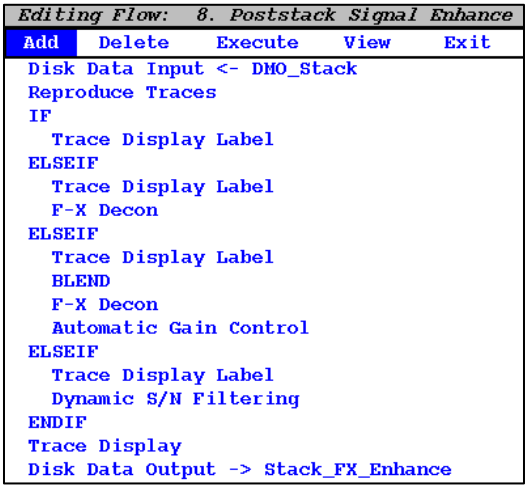

Figure 30: Post-Stack Signal Enhancement Flow
Flow outlining processes and operators used for Post-Stack Enhancement. Screenshot from ProMAX.

4.8.1 F-X Deconvolution

F-X deconvolution (Figure 31) is designed to attenuate random noise by applying a Fourier transform to each trace of the stacked section (Burger et al., 2006; Reynolds, 2011). This type of deconvolution outputs a stacked section with less random noise than possessed by the input data. The Fourier transform converts the data from time and distance to frequency and distance, transforming a time slice to a frequency slice (Gülünay, 2003; Waters, 1987). Events with similar dips are recorded in the frequency slice and F-X Deconvolution uses a Wiener filter to predict the signal one trace ahead (Gülünay, 1986; Treitel, 1974). Any deviation from the predicted and actual signal is removed (Gülünay, 1986; Treitel, 1974).

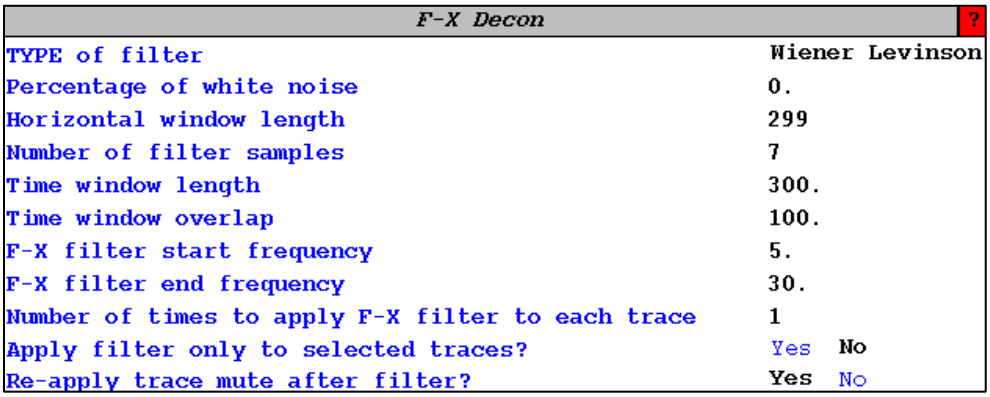

Figure 31: F-X Decon Process
Parameters used in the F-X Decon operator to be applied in Post-stack Enhancement. Screenshot from ProMAX.

Figure 31 outlines the parameters used in the F-X Decon operator. Adding a percentage of white noise to the filter will increase the amount of noise reduction but will also sacrifice coherent data in that reduction. No white noise is added to the filter in this operator. Horizontal window length corresponds with the number of traces in the horizontal F-X prediction window; 299 is the total number of CDPs in the stacked section. 7 filter samples are selected in the prediction filter. A default value of 4 is nearly doubled to account for the conflicting dips in the data due to the highly-faulted study region (Landmark). The time window and length are kept at default values. The F-X filter start and end frequencies are determined by the pre-stack bandpass filter start and end frequency taper values. Default parameters are used for the final three operators. Figure 32 is the stacked section with the F-X deconvolution filter applied.

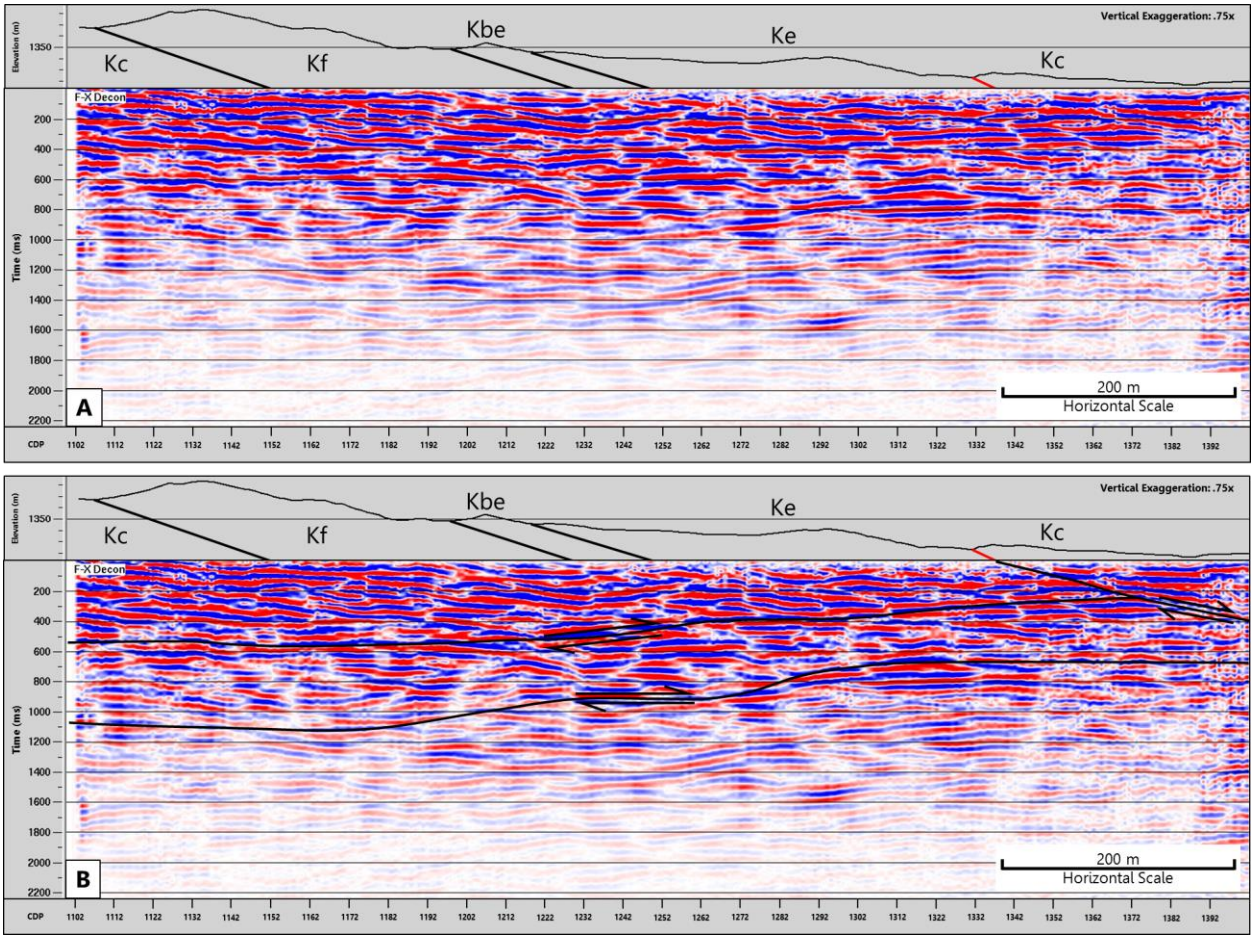

Figure 32: F-X Decon Enhanced Ensemble Stack
Explosive dataset F-X deconvolution post-stack signal enhancement ensemble stack with topographic profile, approximate dip and lithological contacts labeled and indicated by black lines. Kcx defines Cox Sandstone, Kf defines Finlay Formation, Kbe defines Benevides Formation, Ke defines Espy Limestone. Panel A: Uninterpreted stack. Panel B: Interpreted stack, where red and black contact indicates Bennett Thrust Fault in northeast pat of the stack and black lines indicate deeper faulting. Screenshot from ProMAX.

4.8.2 F-X Deconvolution Blend

The previously described F-X deconvolution (Figure 31) is used in conjunction with the Blend operator (Figure 33). The Blend operator uses the output from the F-X Decon operator and combines it with a ratio of the input data. This operator allows maximum flexibility and reduces some of the effects of the operator it is implemented with. Figure 34 shows the effect of the Blend operator on the F-X Decon ensemble stack.

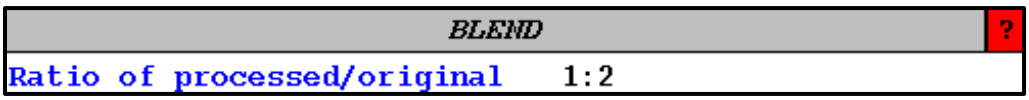

Figure 33: Blend Process
Parameter used in the Blend operator used in conjunction with the F-X Decon operator to be applied in Post-stack Enhancement. Screenshot from ProMAX

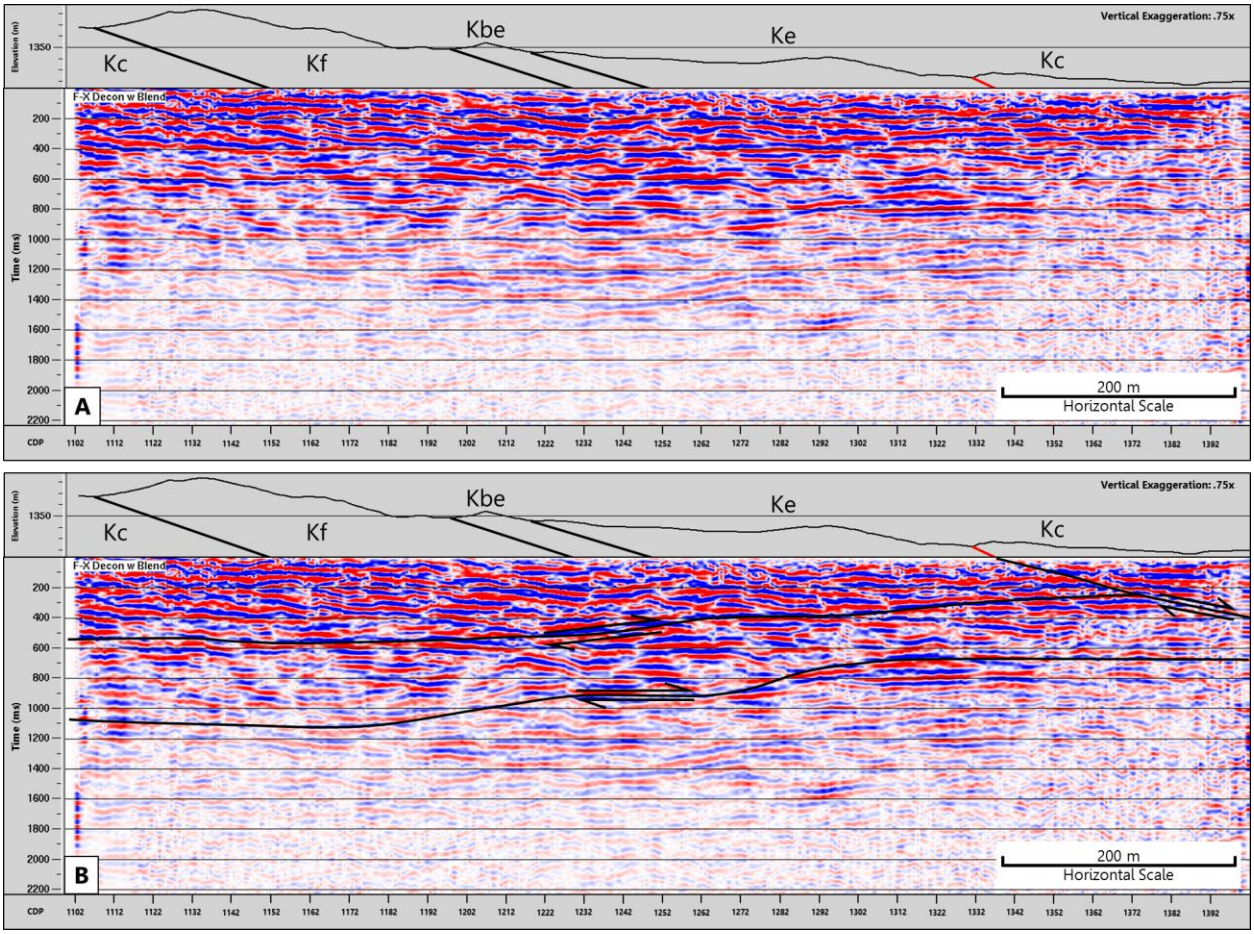

Figure 34: F-X Decon with Blend Enhanced Ensemble Stack
Explosive dataset F-X deconvolution with blend post-stack signal enhancement ensemble stack with topographic profile, approximate dip and lithological contacts labeled and indicated by black lines. Kcx defines Cox Sandstone, Kf defines Finlay Formation, Kbe defines Benevides Formation, Ke defines Espy Limestone. Panel A: Uninterpreted stack. Panel B: Interpreted stack, where red and black contact indicates Bennett Thrust Fault in northeast part of the stack and black lines indicate deeper faulting. Screenshot from ProMAX

4.8.3 Dynamic S/N Filtering

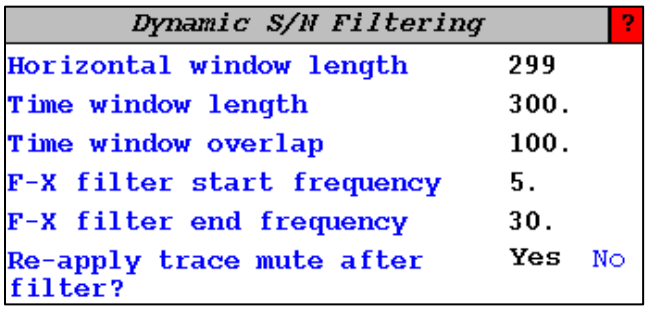

Figure 35: F-X Decon with Blend Enhanced Ensemble Stack
Parameters used in the Dynamic S/N Filtering operator to be applied in Post-stack Enhancement. Screenshot from ProMAX.

Figure 35 outlines the operators used in the Dynamic S/N (Signal to Noise) Filtering operator. The same applicable parameters are defined and used in this filtering operator as the previously described F-X Decon operator (Figure 35). Similar to F-X deconvolution, Dynamic S/N Filtering transforms data from time to frequency and enhances the lateral coherency of the stack by weighting each frequency within the specified frequency window by a function derived from the signal-to-noise ratio of the surrounding traces of the target trace in the stack (Figure 36) (Canales, 1984; Gülünay, 1986; Landmark). However, the S/N filtering technique differs from that of the F-X deconvolution technique; it applies an amplitude only convolutional filter to each trace individually, so there is no "lateral smearing" of traces. F-X deconvolution filtering technique uses a predictive technique and invokes elements from neighboring traces (Canales, 1984; Gülünay, 1986; Landmark). Figure 37 is the stacked section with the Dynamic S/N Filter applied.

$$Weight\ (f) = \frac{S(f)^2}{S(f)^2 + N(f)^2}$$

Figure 36: Dynamic S/N Filtering Equation
Equation calculating the frequency domain weighting filter, where Weight (f) is equal to the signal-to-noise weighting factor, S(f) is equal to the trace signal frequency and N(f) is equal to the trace noise frequency (Landmark).

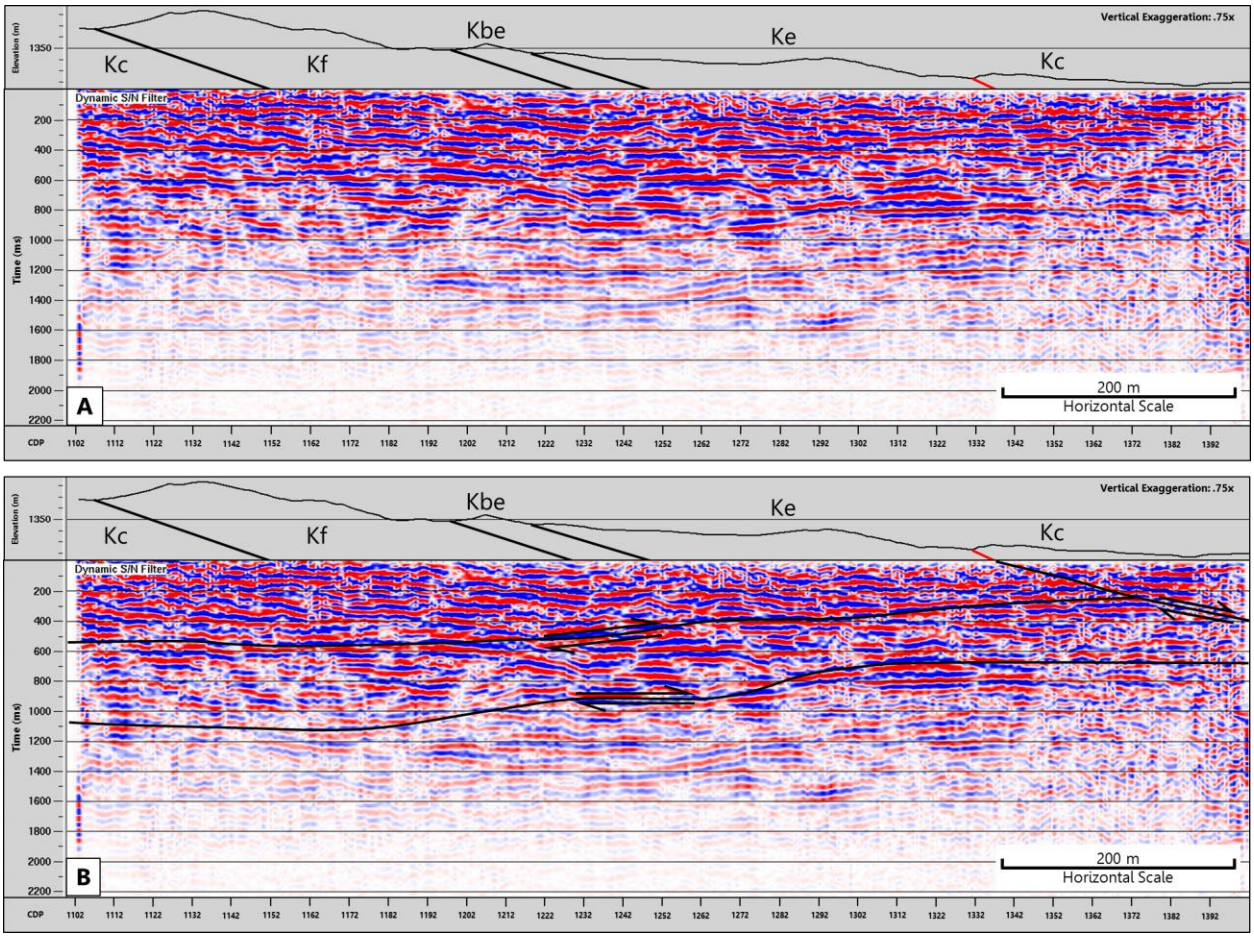

Figure 37: Dynamic S/N Filter Enhanced Ensemble Stack
Explosive dataset S/N filtering post-stack signal enhancement ensemble stack with topographic profile, approximate dip and lithological contacts labeled and indicated by black lines. Kcx defines Cox Sandstone, Kf defines Finlay Formation, Kbe defines Benevides Formation, Ke defines Espy Limestone. Panel A: Uninterpreted stack. Panel B: Interpreted stack, where red and black contact indicates Bennett Thrust Fault in northeast part of the stack and black lines indicate deeper faulting. Screenshot from ProMAX.

4.9 VELOCITY MANIPULATION

The Velocity Manipulation operator in ProMAX converts RMS, interval, average, and residual functions in time or depth into other types of velocity functions. This operator is necessary in this processing flow in order to convert the stacking (RMS) velocity table, picked in Section 4.4: Velocity Analysis, to an average velocity table in depth (Figure 38). The RMS to interval conversion used is the Smoothed gradients option, which outputs a conversion consisting of continuous first derivatives and has a smooth variation in slope. The time-step sizes for the output velocity table refers to the increment (in milliseconds) that a smooth RMS to interval conversion takes place. The output velocity table, "vel", is used in the next and final process.

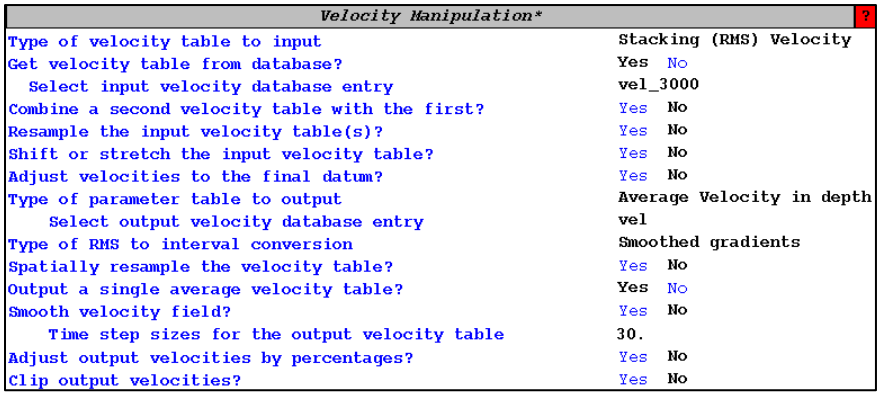

Figure 38: Velocity Manipulation Process
Parameters used in Velocity Manipulation. Screenshot from ProMAX.

4.10 TIME-TO-DEPTH CONVERSION

The Time/Depth Conversion operator converts the input stacked section from two-way-travel time to depth and vice versa. The input data from Section 4.8: Post-stack Enhancement is the enhancement output that results from the F-X Decon (Figure 39). The conversion direction used in the Time/Depth Conversion is Time-to-Depth (Figure 40) and the maximum coherency frequency of interest (in Hz) is 50 (Figure 19). The percent velocity scale factor refers to the appropriate percent at which to multiply all velocities. A value of 100% leaves the velocities in the table untouched and unaltered (Landmark). Figure 41 is the stacked section once the time-to-depth conversion has taken place.

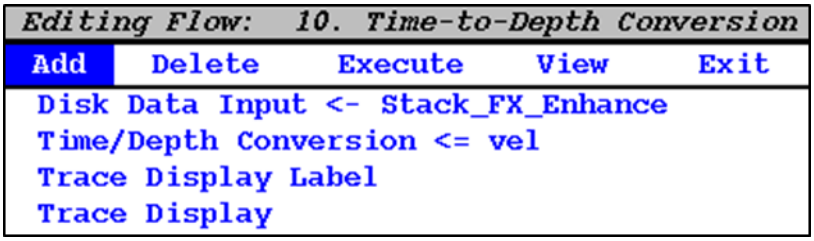

Figure 39: Time to Depth Conversion Flow
Flow outlining processes and operators used for Time-to-Depth Conversion. Screenshot from ProMAX.

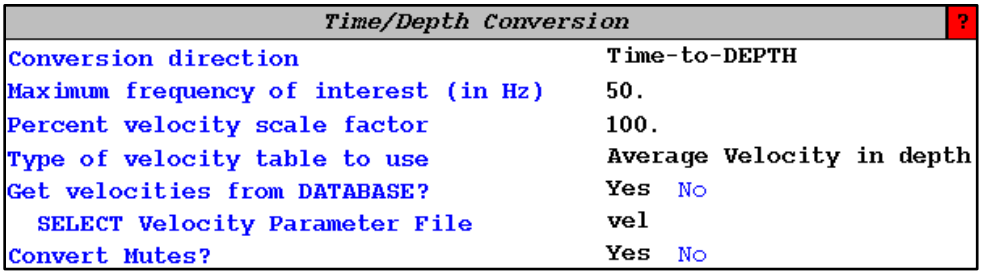

Figure 40: Time/Depth Conversion Process
Parameters used in the Time/Depth Conversion operator to be applied in Time-to-Depth Conversion. Screenshot from ProMAX.

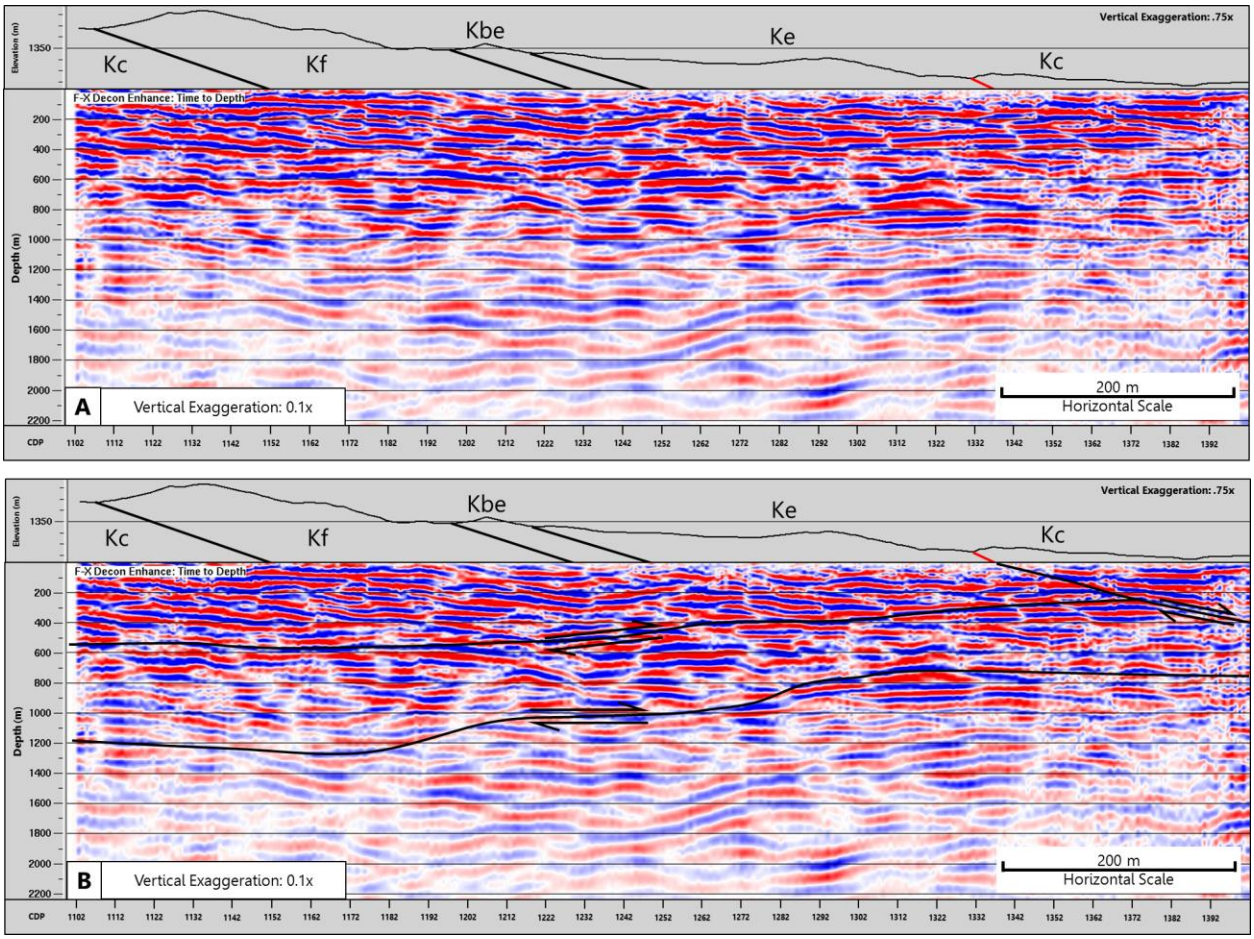

Figure 41: Time-to-Depth Converted Ensemble Stack
Explosive dataset migrated ensemble stack using F-X Decon Stack with topographic profile, approximate dip and lithological contacts labeled and indicated by black lines. Kcx defines Cox Sandstone, Kf defines Finlay Formation, Kbe defines Benevides Formation, Ke defines Espy Limestone. Panel A: Uninterpreted stack. Panel B: Interpreted stack, where red and black contact indicates Bennett Thrust Fault in northeast part of the stack and black lines indicate deeper faulting. Screenshot from ProMAX

5. Results and Discussion

We observed several differences between each dataset, based on quantitative and qualitative observations. Frequency content in the explosive dataset is much lower than that of the hammer dataset; the dominant frequency in the explosive dataset is 14 Hz and the dominant frequency in the hammer dataset is 54 Hz (Figure 10). This difference in frequency content is

directly related to the source type, depth of penetration and the signal-to-noise ratio (Baker, 1999; Feroci et al., 2000). Strong, clear, and coherent reflectors are observed down to 1000 ms in the explosive dataset, and if an average velocity of 2000 m/s is assumed, reaches a depth of 2000 m (Figure 12). This depth is consistent with the time-to-depth converted image (Figure 41). However, in the higher frequency hammer dataset, strong, clear, and coherent reflectors are observed down to 600 ms and if an average velocity of 2000 m/s is assumed, reaches a depth of 1200 m (Figure 12). Additionally, even after trace editing and parameter selection, the hammer dataset is still quite noisy, particularly at longer offsets (Figure 12). This could be attributed to the larger bandwidth of allowable frequencies in the bandpass filter (Figure 10) and that the sledgehammer does not generate or propagate as much energy as the explosive source does to far offset receivers.

First arrivals are clearly observable on shot gather 150 (Figure 12) from one end of the line to the other for the explosive sourced dataset and out to approximately 50 m for the hammer sourced dataset. The lack of coherent phase arrivals at longer offsets makes it difficult to identify bad traces at those longer offsets, which is why four times as many killed traces were identified in the explosive dataset compared to the hammer dataset (Figure 12).

Figure 17 shows the velocity spectra of both the explosive and hammer datasets at CDP 1278, which is approximately positioned two-thirds of the way from the southwest end of the survey line. The wavelets of the explosive and hammer datasets vary in amplitude (Figure 11, Figure 12, Figure 17 and Figure 42). As stated previously, the frequency spectra for each dataset (Figure 10) vary significantly, which influences the amplitudes present in the dataset; frequency and amplitude are inversely related. These lower amplitudes coupled with the incoherent noise made it extremely difficult to pick appropriate velocities in the hammer dataset, which led to the

inability to produce a reasonable CDP stacked image for full interpretation (Figure 42). However, the reflection fabric in the upper 500 m of the hammer sourced ensemble stack may reflect the layer that is interpreted as the first fault in the explosive sourced dataset. Future pre-stack processing methods may be implemented to mitigate these issues to produce a CDP stacked image using the hammer dataset. The following processes should be considered.

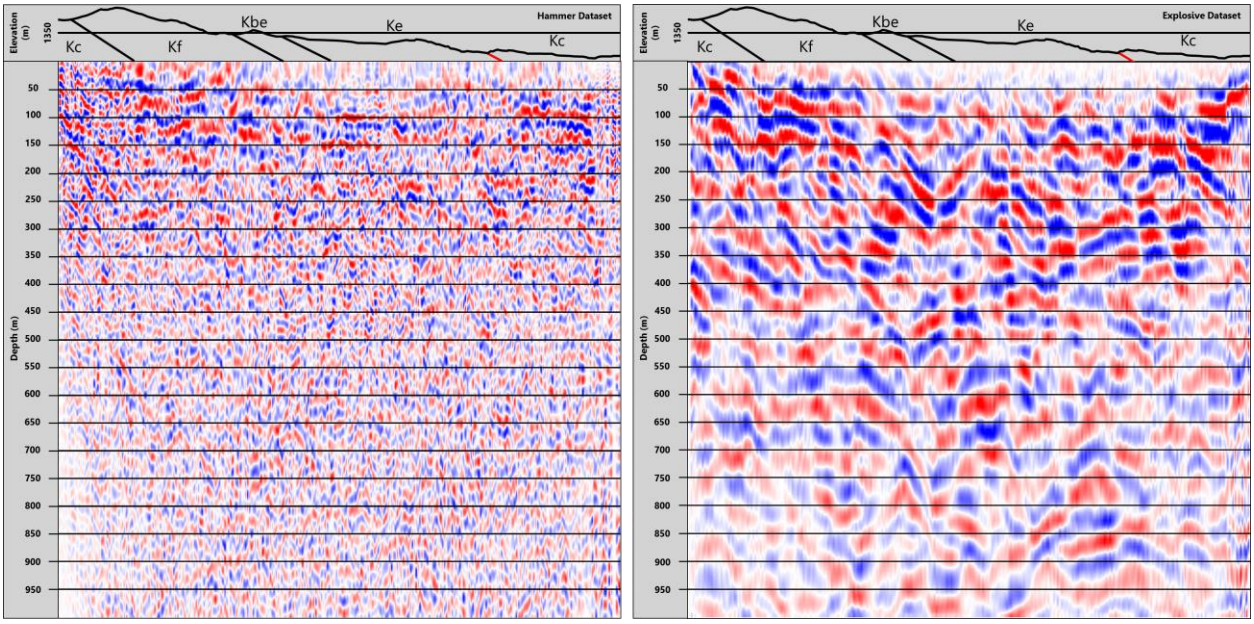

Figure 42: 1:1 Hammer and Explosive Dataset Ensemble Stacks
Hammer and Explosive dataset migrated ensemble stacks using F-X Decon Stack with topographic profile, approximate dip and lithological contacts labeled and indicated by black lines. Kcx defines Cox Sandstone, Kf defines Finlay Formation, Kbe defines Benevides Formation, Ke defines Espy Limestone. Screenshot from ProMAX

1. Use only near offset receivers from each gather in subsequent processing, as frequency and noise content change away from the shot location (Feroci et al., 2000).

2. Define appropriate deconvolution gate. Processing artifacts may be present due to inadequate or inappropriate deconvolution. Deconvolution of shallow reflection data almost always degrades the quality of reflections (Steeples and Miller, 1998).

3. Implement time-variant spectral whitening to more accurately and precisely mitigate the effects of ambient noise and airwave associated noise (Figure 43) (Campbell et al., 2010; Treeby, 2013; Yilmaz, 2001).

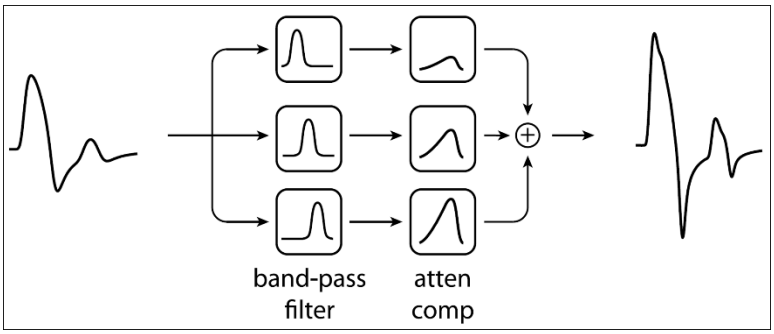

Figure 43: Time-Variant Spectral Whitening Schematic
Schematic of time-variant spectral whitening technique, in which the seismic trace is filtered using a series of narrow bandpass filters and convolved with attenuation-compensation operators (Yilmaz, 2001).

The explosive dataset was successful in producing a stacked image that I interpreted, starting with the initial NMO Stack (Figure 19) and ending with a migrated stacked image (Figure 41) with two possible interpretations (Figure 44 and Figure 45). Figure 44 incorporates a more complex anticline-syncline fold geometry to explain the fabric of reflections, whereas Figure 45 interprets the fabric of near-surface reflections as processing artifacts.

Starting with the initial stack and moving onto the next stack, DMO Stack (Figure 19 and Figure 29), the difference in coherent reflectors or faulting events is negligible. However, following the NMO and DMO processes, the post-stack signal enhancement process yielded the greatest advancement in resolving the clarity of the stacked image. Three post-stack signal enhancement methods were tested: F-X deconvolution, F-X deconvolution with a blend operator, and Dynamic S/N filtering. The signal enhancement method that produced the clearest and coherent image was the F-X deconvolution, so this is the stacked image that is used moving forward in the flow and in time-to-depth migration. The Blend operator uses an input ratio of the

processed and original data. In this study, a ratio of 1:2 was used and tested, and produced a stack that was not as clear and not as coherent as using only the F-X deconvolution. The Blend operator is a useful tool that preserves a desired amount of the original data. A smaller ratio could yield a clearer and better image to move forward with, however for the scope and scale of this project, the F-X deconvolution operator without the Blend operator is sufficient. Dynamic S/N filtering applies a filter to each individual trace based on the signal to noise ratio of that trace, whereas F-X deconvolution predicts the signal one trace ahead, based on the characteristic of the preceding trace. This leads to less mixing or lateral smearing of data from trace to trace. However, the purpose of this study is to interpret faulting location; fault features will appear where trace signals aren't similar to one another and will not appear where trace signals are similar, therefore mixing and lateral smearing of data is allowed to make faults more apparent (Fehmers and Höcker, 2003).

5.1 STRUCTURAL INTERPRETATION OF REFLECTION IMAGES

Figure 44, Figure 45 and Figure 46 show the interpreted migrated stacked image without any vertical or horizontal exaggeration. The observed dip directions for most of the reflections in the three interpretations, which I interpret as the interbedded layers in the near-surface, Cretaceous sedimentary rocks, are between 20° and 30° northeast (Figure 44.A, Figure 45.A and Figure 46.A), which is consistent with the dip measurements taken in the field (Langford and Pavlis) (Figure 48). The dip of the Bennett Thrust Fault is approximately 45°, which is also consistent with dip measurements in the seismic data near the surface location of the Bennett Thrust (Figure 44.C, Figure 45.C, Figure 46.C, Figure 47 and Figure 48).

Additional thrust horses have been interpreted as well, indicated by the brown shades, which I have named the Dixie Thrust horse (DH) and the Trixie Thrust horse (TH), in Figures 44 and 45. Without exposure of these horses at the surface, I cannot determine which lithological units comprise them and what their lithological geometries may be, but I hypothesize that both DH and TH would be comprised of a similar, repetitive section of rock, much like the Bennett Thrust horse, starting with the oldest formation, the Yucca Formation, and ending with the youngest, the Espy Limestone. However, the structural components of each newly found horse can be interpreted in each of the interpreted stacked images. Both the Dixie and Trixie Thrust Faults are interpreted as reactivated normal faults formed during the initial basin formation; both faults have a dip ranging from 30° to 40°, which is consistent with physical modeling and analogous regions (Beauchamp et al., 1996; Kley et al., 2005; Konstantinovskaya et al., 2007; Mora et al., 2009). In Figures 44 and 45, DH and TH are interpreted the same way. DH exhibits the classic ‘S’ shape of an anticline syncline pair (Figure 44.B and Figure 45.B); the leading anticline is a ramp anticline, which is the result of the horse climbing over the footwall ramp,

and the tailing syncline is the result of the horse conforming to the footwall ramp base of the Bennett Thrust horse. In order to produce the anticline-syncline pair in the Bennett Thrust horse in Figure 44.D and Figure 45.D, one of two things must be present: either a blind back thrust would have to be present, which are common in basin inversion (Figure 44.E), or a detachment surface bounding the anticline-syncline pair would have to be present to allow accommodation space for folds (Figure 45.E). Either are possible, however Figure 45 would be less likely due to the lack of surface manifestation of that detachment surface, given how close these folds are to the surface in the interpretation. The second, alternative interpretation does not include these complex fold geometries, and interprets the apparent folded fabric of those units as being caused by processing artifacts (Figure 46.D). Artifacts such as those could be produced by noise or could be related to uncertainties and challenges in velocity analysis (such as using incorrect replacement velocity in the elevation static correction or picking incorrect velocities during the RMS velocity picking) and DMO binning. The second interpretation is simpler, but I am confident that the appropriate parameters were selected for each step in the processing flow, so the first interpretation (Figure 44) represents my preferred model for subsurface structural and lithological geometries.

Figure 47 displays the interpretation from Figure 44 with interval velocities overtop from the same 4 CDP locations along the line from Figure 20. Both CDP 1137 and CDP 1207 show peak interval velocity reversals at approximately 550 m that correspond with the interpreted geometry of the Dixie Thrust Fault, with the transition from the Cox Sandstone to the Dixie Horse, and CDP 1278 shows a slight interval velocity increase at approximately 425 m, corresponding with that same transition. Both CDP 1278 and CDP 1342 show peak interval velocity reversals at approximately 850 m and 650 m, respectively. These reversals correspond

with the interpreted geometry of the Trixie Thrust Fault, with the transition from the Dixie Thrust Horse to the Trixie Thrust Horse. Using interval velocity analysis in this way helps to constrain the geometric interpretations of structural features in the subsurface.

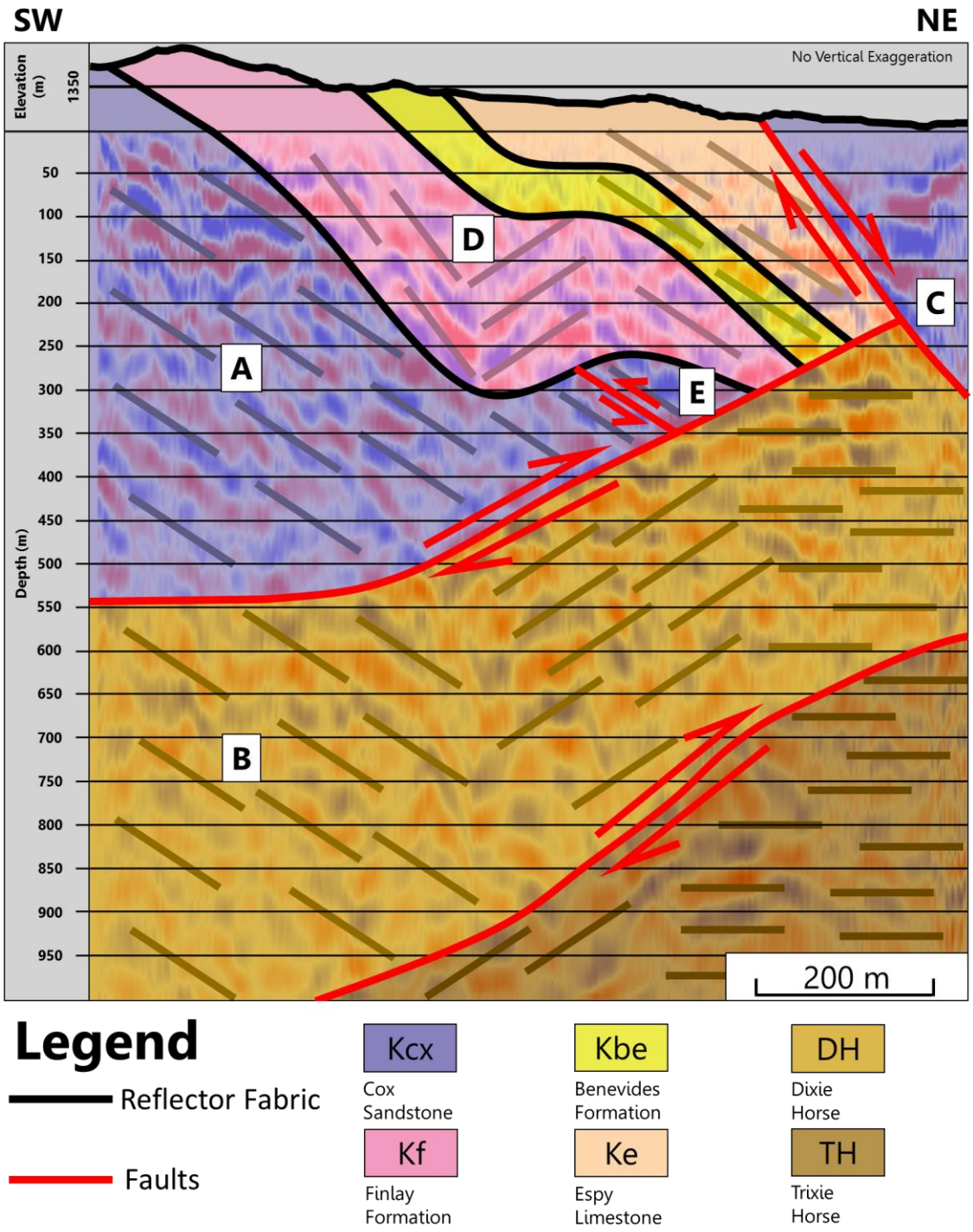

Figure 44: 1:1 Explosive Dataset Time to Depth Converted Interpreted Ensemble Stack 1 Explosive dataset migrated ensemble displaying no vertical exaggeration, topographic profile, approximate dip and lithological contacts, and fault interpretations. Caption A: Indicating 20°-30° dipping reflector fabric. Caption B: Indicating anticline-syncline pair in newly interpreted thrust horses. Caption C: Indicating Bennett Thrust Fault. Caption D: Indicating anticline-syncline pair in Bennett Thrust Horse. Caption E: Indicating back thrust. Screenshot from ProMAX.

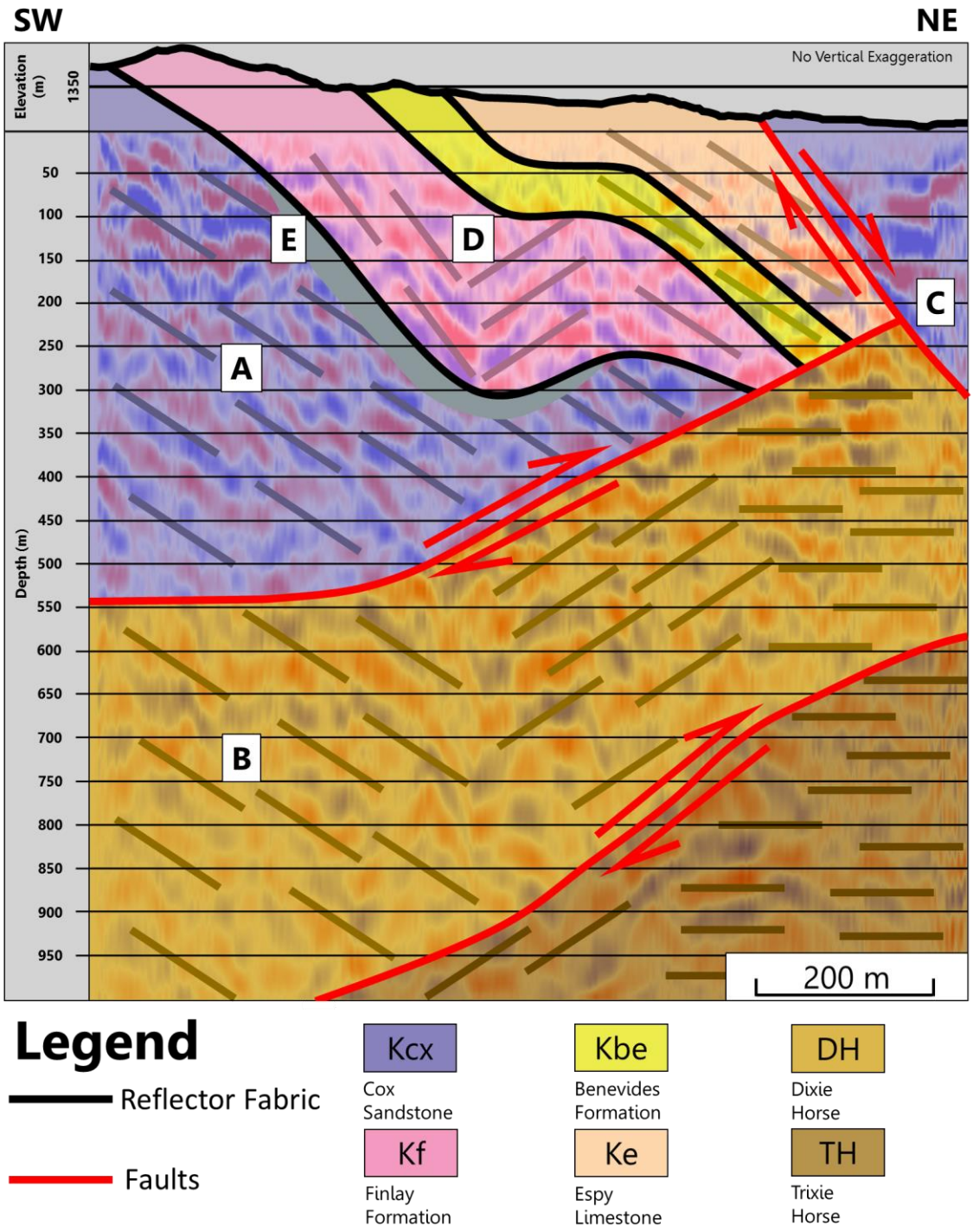

Figure 45: 1:1 Explosive Dataset Time to Depth Converted Interpreted Ensemble Stack 2 Explosive dataset migrated ensemble displaying no vertical exaggeration, topographic profile, approximate dip and lithological contacts, and fault interpretations. Caption A: Indicating 20°-30° dipping reflector fabric. Caption B: Indicating anticline-syncline pair in newly interpreted thrust horses. Caption C: Indicating Bennett Thrust Fault. Caption D: Indicating anticline-syncline pair in Bennett Thrust Horse. Caption E: Indicating detachment zone. Screenshot from ProMAX.

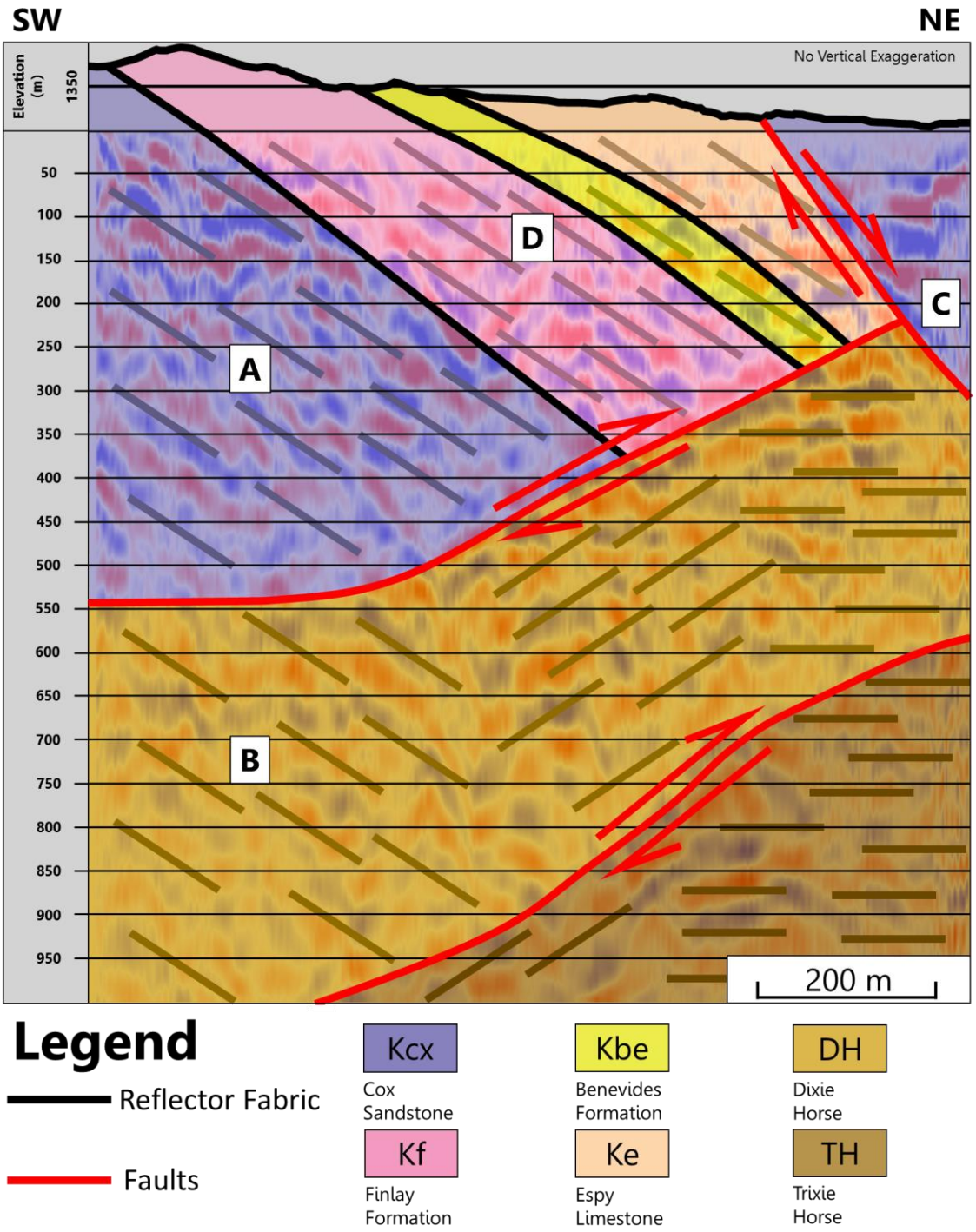

Figure 46: 1:1 Explosive Dataset Time to Depth Converted Interpreted Ensemble Stack 3 Explosive dataset migrated ensemble displaying no vertical exaggeration, topographic profile, approximate dip and lithological contacts, and fault interpretations. Caption A: Indicating 20°-30° dipping reflector fabric. Caption B: Indicating anticline-syncline pair in newly interpreted thrust horses. Caption C: Indicating Bennett Thrust Fault. Caption D: Indicating processing artifact in Bennett Thrust Horse. Screenshot from ProMAX.

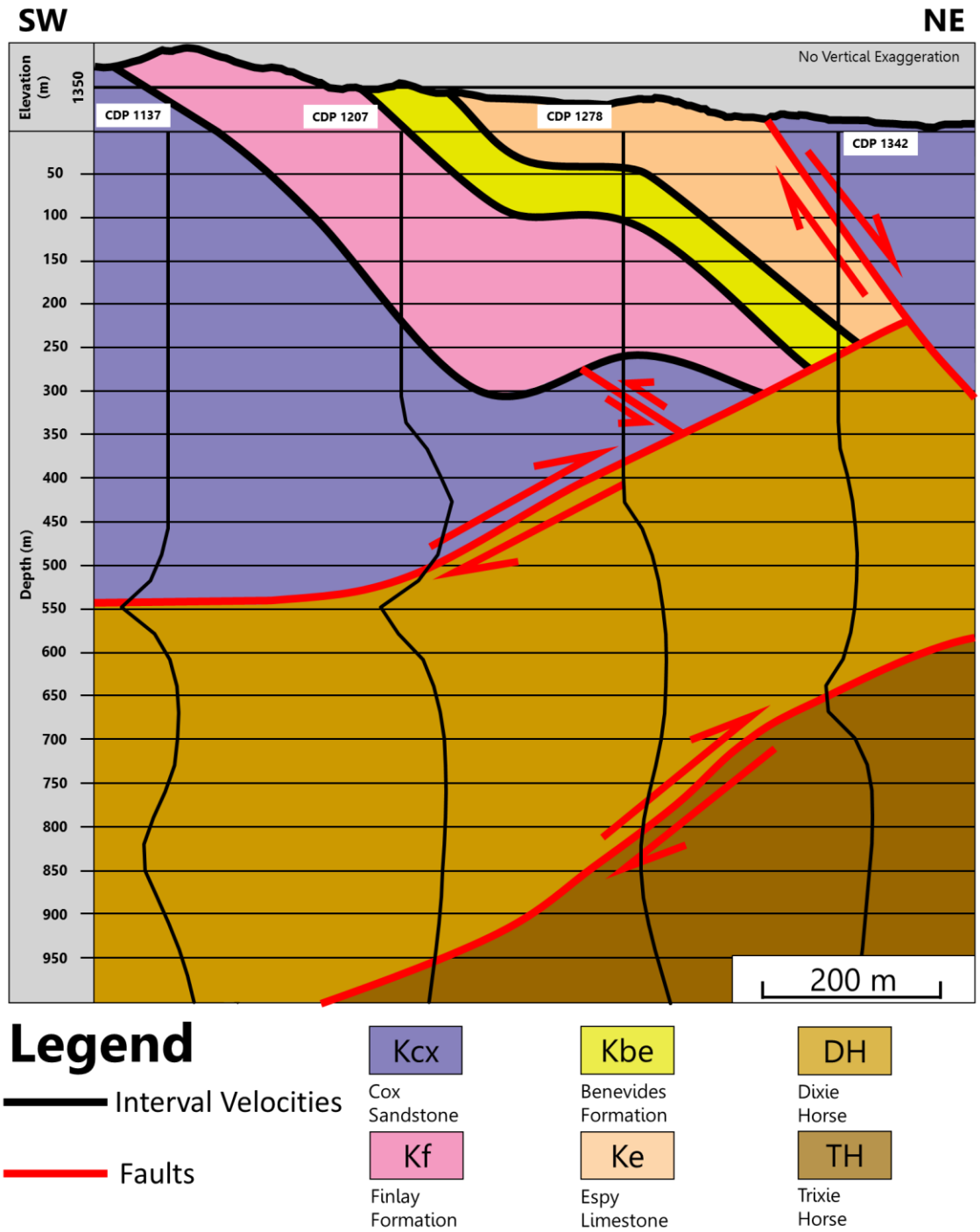

Figure 47: 1:1 Time to Depth Converted Interpreted Ensemble Stack with Interval Velocities Explosive dataset migrated ensemble displaying no vertical exaggeration, topographic profile, approximate dip and lithological contacts, fault interpretations and relative interval velocities. Screenshot from ProMAX.

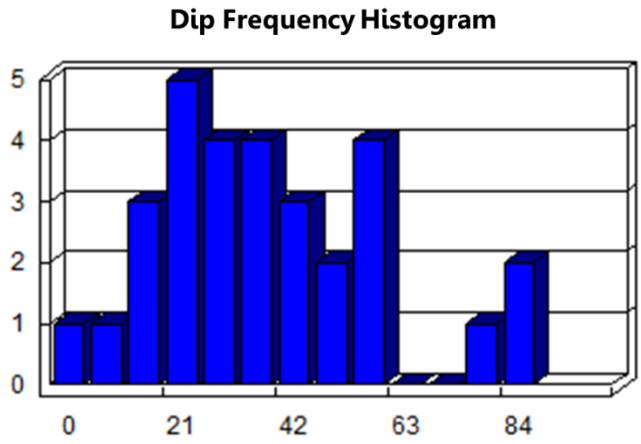

Figure 48: Dip Frequency Histogram
Histogram showing the concentrations of bedding dips in the region of 30 field measurements (Langford and Pavlis). Screenshot from ArcGIS.

In order to assess whether or not I could expect to see reflections from various lithological boundaries, I observed velocities from the data and estimated densities to calculate the reflection coefficients (RC) of each lithologic unit and contact. Table 2 displays velocities, densities and RCs of each lithologic unit and contact, along with a labeled topographic profile for reference. Velocity values are populated from the first datum point of each of the four 1-D velocity profiles in Figure 19 and density values are populated from approximate average densities (Reynolds, 2011). The reflection coefficient of a lithological interface is a ratio of energy of the reflected wave and the incident wave, which is dependent on the velocities and densities of the lithological units at that interface (Figure 49). A reflection coefficient closer to ±1 indicates more energy is reflected than transmitted and a reflection coefficient and a reflection coefficient closer to 0 indicates more energy is transmitted than reflected (Reynolds, 2011; Waters, 1987). Reflection coefficients present in this study indicate that there is little contrast in acoustic impedance across lithological interfaces (-0.12 to 0.17 range in calculated RCs), so I expect that those boundaries would not produce strong reflections and make them hard to identify within the seismic reflection

images. This is consistent with observations in the data, with no strong reflections from dipping sedimentary layer boundaries, presented in Table 2.

Table 2: Reflection Coefficient Table
Table with velocities, approximate average densities of lithological units and reflection coefficients calculated for the interfaces between those units. Velocities populated from first datum point in 1-D Velocity Profiles (Figure 20) and densities populated from Reynolds (2011). Labeled topographic profile for reference. Kcx defines Cox Sandstone, Kf defines Finlay Formation, Kbe defines Benevides Formation, Ke defines Espy Limestone.

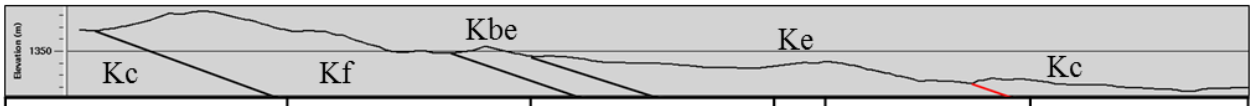

Lithological Unit	Velocity (m/s)	Density (g/cc)		Interface	RC
Kcx	2200	2.35		Kcx/Kf	-0.12
Kf	2600	2.55		Kf/Kbe	0.17
Kbe	2000	2.35		Kbe/Ke	0.01
Ke	1800	2.55		Ke/Kcx	-0.06

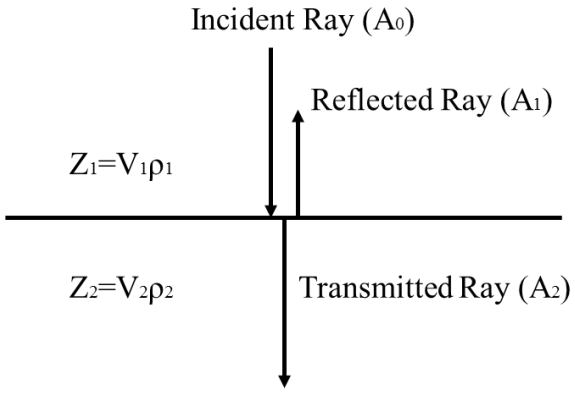

$$RC = \frac{(Z_2 - Z_1)}{(Z_2 + Z_1)}$$

Figure 49: Reflection Coefficient Schematic
Simple schematic for the partitioning of energy of an incident ray, reflected ray and downward-transmitted ray at a lithological interface. Equation for calculating the reflection coefficient of a lithological interface. Modified from Reynolds, 2011.

6. SUMMARY & CONCLUSIONS

For this thesis, I designed, acquired, processed and interpreted a 1-km-long explosive-source and hammer-source, 2-D reflection seismic line in the Indio Mountains of West Texas. I produced migrated CDP stacks using reflection processing methods for the explosive-source and hammer-source datasets. The data quality of the hammer-source reflection image (Figure 42) made it difficult to interpret, so I focused on interpreting the explosive-source reflection image (Figure 42). The Bennett Thrust Fault is able to be identified and interpreted, as well as hypothesized additional imbricate fault structures, the Dixie and Trixie Thrust Faults (Figure 44). The additional imbricate faulting identified in this study is consistent with the hypothesis of Page (2011) based on his structural reconstruction modeling. The presence of these hypothesized structures sheds light on the structural styles and kinematics of basin inversion present in the region. Additionally, this study provides a different perspective on the structures present in an inverted rift basin and the scale at which the data were collected is unique. Published papers that seismically investigate and reconstruct the structural and lithological geometries of an inverted rift basin involve large and expansive surveys, with survey lines ranging from 10 km to 100+ km (Beauchamp et al., 1996; Mora et al., 2009; Navarrete et al., 2015). A survey consisting of a 2-D line that is only 1 km with narrow shot and receiver spacing, provides a localized and more detailed look at the structures and style of deformation present in the folded shoulder of an inverted rift basin.

The Chihuahua Trough formed approximately 159-156 mya, and lies on the southern part of the North American craton along the United States and Mexico border (Rohrbaugh, 2001; Haenggi, 2002; Carciumaru and Ortega, 2008). The Cretaceous aged stratigraphy that the study encompassed records a depositional transition, from a terrestrial rift basin to marine transgressive sequence (Haenggi, 2002; Page, 2011). Laramide Orogeny related contraction reactivated basinal extension faults and inverted the Chihuahua Trough. This inversion produced the Bennett Thrust Fault, the newly interpreted anticline-syncline pair in the Bennett Thrust horse, and the newly

interpreted Dixie and Trixie horses below. The third and final period of tectonic activity present in the region occurred in the Neogene, and produced the Indio Fault, which exposes the easterly dipping beds and exposes the north-easterly dipping beds that are present today.

The three major phases of tectonic activity present in the Indio Mountains result in a complicated and complex mountain range. Further seismic and non-seismic geophysical studies should be conducted in the future to better constrain the subsurface structural and lithological geometries (Hesthammer, 1999). These further studies will yield greater insight on the styles and extent of deformation present in the Indio Mountains near the UTEP Field Station.

REFERENCES

Baker, G.S., 1999, Processing near-surface seismic-reflection data: A primer: Society of Exploration Geophysicists, http://library.seg.org/doi/abs/10.1190/1.9781560802020 (accessed March 2017).

Beauchamp, W., Barazangi, M., Demnati, A., and El Alji, M., 1996, Intracontinental rifting and inversion: Missour basin and Atlas mountains, Morocco: AAPG bulletin, v. 80, p. 1459–1481.

Bekara, M., and van der Baan, M., 2009, Random and coherent noise attenuation by empirical mode decomposition: GEOPHYSICS, v. 74, p. V89–V98, doi: 10.1190/1.3157244.

Burger, H.R., Sheehan, A.F., and Jones, C.H., 2006, Introduction to Applied Geophysics: Exploring the Shallow Subsurface: W.W. Norton & Company, 554 p.

Campbell, F.M., Kaiser, A., Horstmeyer, H., Green, A.G., Ghisetti, F., Gorman, A.R., Finnemore, M., and Nobes, D.C., 2010, Processing and preliminary interpretation of noisy high-resolution seismic reflection/refraction data across the active Ostler Fault zone, South Island, New Zealand: Journal of Applied Geophysics, v. 70, p. 332–342, doi: 10.1016/j.jappgeo.2009.05.001.

Canales, L.L., 1984, Random Noise Reduction: SEG Technical Program Expanded Abstracts 1984, p. 525–527.

Carciumaru, D., and Ortega, R., 2008, Geologic structure of the northern margin of the Chihuahua trough: Evidence for controlled deformation during Laramide Orogeny: Boletín de la Sociedad Geológica Mexicana, v. 60, p. 43–69.

Castle, R.J., 1994, A theory of normal moveout: Geophysics, v. 59, p. 983–999.

DeFord, R., 1969, Some keys to the geology of northern Chihuahua, *in* The Border Region (Chihuahua, Mexico, & USA), New Mexico Geological Society Field Conference Guidebook 20, p. 228.

Deregowski, S.M., 1986, What is DMO? First Break, v. 4, p. 7–24, doi: 10.3997/1365-2397.1986014.

Dickinson, W.R., and Lawton, T.F., 2001, Carboniferous to Cretaceous assembly and fragmentation of Mexico: Geological Society of America Bulletin, v. 113, p. 1142–1160.

Feroci, M., Orlando, L., Balia, R., Bosman, C., Cardarelli, E., and Deidda, G., 2000, Some considerations on shallow seismic reflection surveys: Journal of Applied Geophysics, v. 45, p. 127–139.

Fox, M.R., 2016, Sedimentologic and stratigraphic analysis of synrift siliciclastic fluvial and lacustrine strata in the Lower Cretaceous upper Yucca Formation, Indio Mountains, West Ttexas: The University of Texas at El Paso.

Gülünay, N., 1986, F-X Decon and the Complex Weiner Prediction Filter for Random Noise Reduction on Stacked Data:.

Gülünay, N., 2003, Seismic trace interpolation in the Fourier transform domain: GEOPHYSICS, v. 68, p. 355–369, doi: 10.1190/1.1543221.

Haenggi, W.T., 2002, Tectonic history of the Chihuahua trough, Mexico and adjacent USA, Part II: Mesozoic and Cenozoic: Boletin de la Sociedad Geologica Mexicana, v. 55, p. 38–94.

Hesthammer, J., 1999, Improving seismic data for detailed structural interpretation: The Leading Edge, v. 18, p. 226–247.

Hunter, J.A., Pullan, S.E., Burns, R.A., Gagne, R.M., and Good, R.L., 1984, Shallow seismic reflection mapping of the overburden-bedrock interface with the engineering seismograph—Some simple techniques: Geophysics, v. 49, p. 1381–1385.

Kattah, S., 2017, Exploration Opportunities in the Pre-Salt Play, Deepwater Campos Basin, Brazil: The Sedimentary Record, v. 15, p. 4–8, doi: 10.2110/sedred.2017.1.

King, P.B., and Flawn, P.T., 1953, Geology and mineral deposits of pre-Cambrian rocks of the Van Horn area, Texas:, https://utexas-ir.tdl.org/handle/2152/27504 (accessed February 2016).

Kley, J., Rossello, E.A., Monaldi, C.R., and Habighorst, B., 2005, Seismic and field evidence for selective inversion of Cretaceous normal faults, Salta rift, northwest Argentina: Tectonophysics, v. 399, p. 155–172, doi: 10.1016/j.tecto.2004.12.020.

Konstantinovskaya, E.A., Harris, L.B., Poulin, J., and Ivanov, G.M., 2007, Transfer zones and fault reactivation in inverted rift basins: Insights from physical modelling: Tectonophysics, v. 441, p. 1–26, doi: 10.1016/j.tecto.2007.06.002.

Landmark, 1998, ProMAX 2D Seismic Processing and Analysis:.

Landmark, 2008, ProMAX Reference:.

Langford, R., and Pavlis, T. Rips “Good” Map: ArcGIS, scale Written Correspondence.

Li, X., 2014, Sedimentologic, stratigraphic, and diagenetic analysis of microbialite-bearing lacustrine rift sequence within the Lower Cretaceous Yucca Formation, Indio Mountains, West Texas: The University of Texas at El Paso.

Mora, A., Gaona, T., Kley, J., Montoya, D., Parra, M., Quiroz, L.I., Reyes, G., and Strecker, M.R., 2009, The role of inherited extensional fault segmentation and linkage in contractional orogenesis: a reconstruction of Lower Cretaceous inverted rift basins in the Eastern Cordillera of Colombia: Basin Research, v. 21, p. 111–137, doi: 10.1111/j.1365-2117.2008.00367.x.

Navarrete, C.R., Gianni, G.M., and Folguera, A., 2015, Tectonic inversion events in the western San Jorge Gulf Basin from seismic, borehole and field data: Journal of South American Earth Sciences, v. 64, p. 486–497, doi: 10.1016/j.jsames.2015.09.012.

Page, S.J., 2011, Fold-thrust system overprinting syn-rift structures on the margin of an inverted rift basin: Indio mountains, west Texas: THE UNIVERSITY OF TEXAS AT EL PASO, http://gradworks.umi.com/15/03/1503742.html (accessed February 2016).

Reynolds, J.M., 2011, An Introduction to Applied and Environmental Geophysics: John Wiley & Sons, Ltd., 696 p.

Rohrbaugh, R., 2001, Contractional and Extensional Deformation Kinematics of the Southern Indio Mountains, Trans-Pecos Texas: The University of Texas as El Paso, 112 p.

Steeples, D.W., and Miller, R.D., 1998, Avoiding pitfalls in shallow seismic reflection surveys: Geophysics, v. 63, p. 1213–1224.

Treeby, B.E., 2013, Acoustic attenuation compensation in photoacoustic tomography using time-variant filtering: Journal of biomedical optics, v. 18, p. 036008–036008.

Treitel, S., 1974, The complex Wiener filter: Geophysics, v. 39, p. 169–173.

Underwood, J.J., 1980, Geology of the Eagle Mountains, Hudspeth County, Texas, *in* Trans Pecos Region (West Texas), Kansas State University, New Mexico Geological Society Field Conference Guidebook 31, p. 308.

Waters, K.H., 1987, Reflection Seismology: A Tool for Energy Resource Exploration: Wiley-Interscience, 538 p.

Yilmaz, O., 2001, Seismic Data Analysis: Processing, Inversion, and Interpretation of Seismic Data: Tulsa, Society of Exploration Geophysicists.

7. APPENDIX

Additionally, P-wave first break picks from all shot gathers of the explosive dataset have been compiled for refraction processing and velocity model construction (Figure 51). Preliminary analysis fits two lines to the slope of the first break picks. Green and yellow lines indicate potential layers to incorporate in the velocity model. The green line has a slope of approximately 2100 m/s (V_1) and the yellow line has a slope of approximately 4200 m/s (V_2). These velocity values fall within the range of picked velocities from Step 4: RMS Velocity Analysis and Picking in the reflection processing flow. Using the depth to refractor equation (Figure 50) a preliminary calculation for shot gather 175 (Figure 51) postulates that with a crossover distance of 325 m, the depth of the interface between the two layers is 94 m at depth. Shot gather 175 is 30 m northeast-offset from the Bennett Thrust Fault. At that surface location, Figures 44, 45, 46 and 47 interpret the Bennett Thrust to be approximately 100 m at depth, which correlates with this preliminary velocity and depth calculation. It should be noted that this velocity calculation and Figure 50 assume flat layer geometries, and due to the complex faulting and folding present in the area, this calculation is not exact. Development of a tomographic P-wave velocity model is beyond the scope of this project. However, a future study could use this pick dataset to invert for a near-surface P-wave velocity model. That velocity model could be compared with my final seismic reflection images and be used to improve velocity models applied for NMO and depth conversion of the reflection images.

$$z = \frac{1}{2} x_c \left[\frac{(V_2 - V_1)}{(V_2 + V_1)}\right]^{1/2}$$

Figure 50: Depth to Refractor Equation
Equation calculating the depth to the refractor of two lithological units, where z is equal to the depth of the refractor, x_c is equal to the crossover distance, V_1 is equal to the velocity of layer 1 and V_2 is equal to the velocity of layer 2 (Reynolds, 2011).

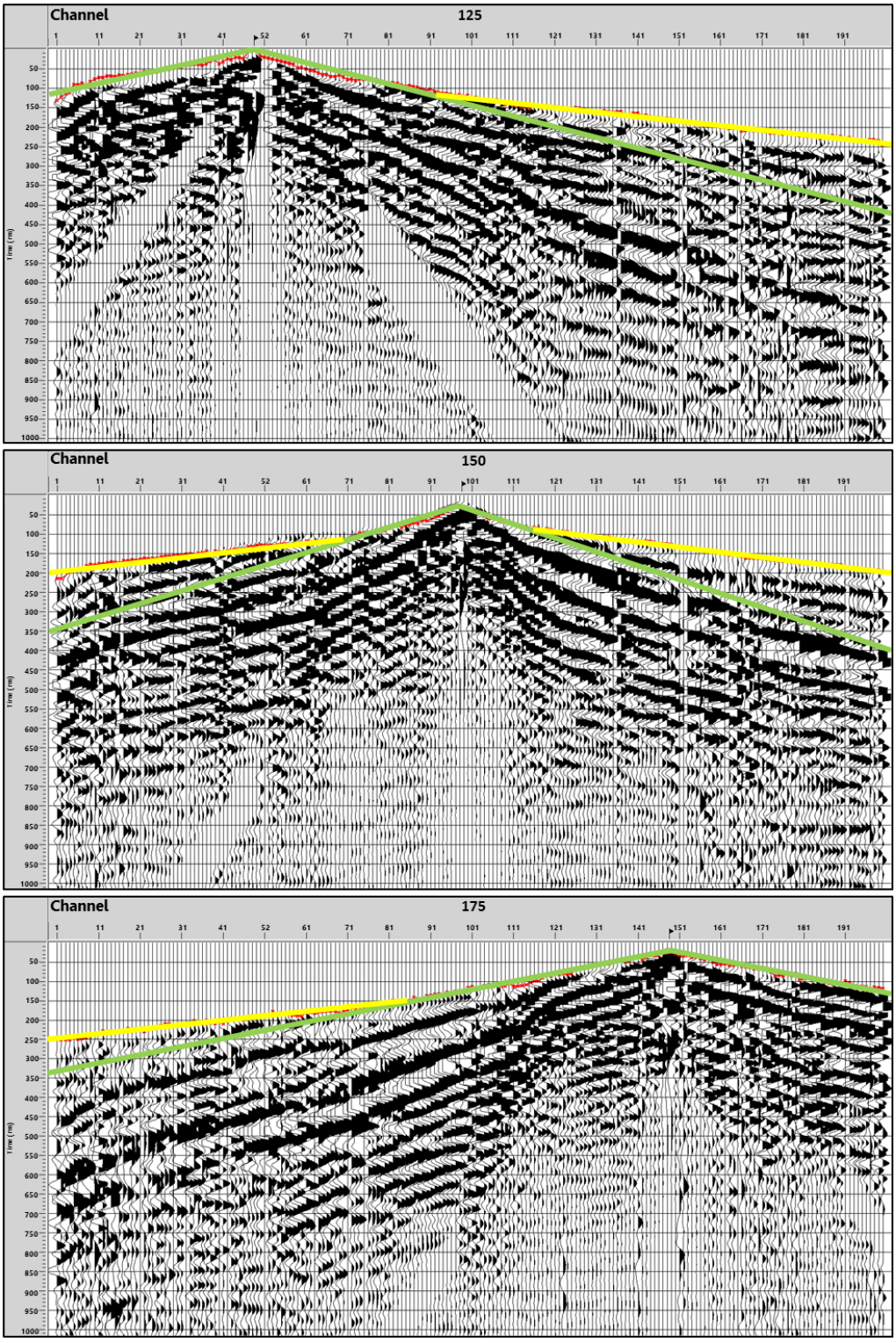

Figure 51: First Break Shot Gathers
Example shot gathers 125, 150, and 175 from the explosive dataset with P-wave first break picks in red after trace editing and parameter selection. Green and yellow lines indicate potential layers to incorporate in refraction velocity model. Screenshots from ProMAX

VITA

Alan Thomas Vennemann was born in Ft. Thomas, Kentucky. Upon graduating from Highlands High School in Ft, Thomas, he entered Northern Kentucky University. In May of 2015, he graduated with a Bachelor of Science in Geology.

In August of 2015 he moved to El Paso to pursue his Master's of Science in Geophysics at University of Texas at El Paso (UTEP). While at UTEP he served as team member for the 2016 American Association of Petroleum Geologists (AAPG) Imperial Barrel Award team, where they took first place internationally out of 176 schools from 42 countries. In May of 2017 he worked as a geoscience intern at Nexen Petroleum U.S.A. in their Eastern Gulf of Mexico Exploration and Development team

After completing his Master's thesis, Alan plans to complete courses necessary for a GIS Certificate in the Spring 2018 semester and move Oklahoma City, OK he will join Chesapeake Energy as a geoscience intern for the summer.

Email: vennemanna1@gmail.com

This thesis was typed by the author, Alan Vennemann.